Chemical Geology 632 (2023) 121537

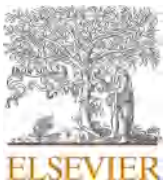

Contents lists available at ScienceDirect

Chemical Geology

journal homepage: www.elsevier.com/locate/chemgeo

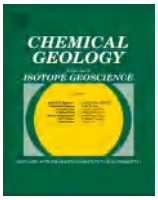

Generation of continental intraplate alkaline basalts by edge-driven convection: Insights from the Cenozoic basalts beyond the Big Mantle Wedge

Liang Zhou, Yu-Ping Su *, Jian-Ping Zheng, Hong-Kun Dai, Qiang Ma, Jian Wang, Sai Zhang, Xia-Hui Zhang, Kai Xiong

School of Earth Sciences, State Key Laboratory of Geological Processes and Mineral Resources, China University of Geosciences, Wuhan 430074, China

ARTICLE INFO

Editor: S Aulbach

Keywords:
Central-East Asia
Intraplate alkaline basalts
Melting mechanism
Thermodynamic modeling
Edge-driven convection

ABSTRACT

Continental intraplate basalts are widespread across Central-East Asia, and their melting mechanisms are poorly known. Herein, we present integrated studies of petrology, elemental-isotope systematics, and thermodynamic modeling of Cenozoic Liangcheng basalts, a representative volcanic field of the vast intracontinental basaltic magmatic province covering Central-East Asia, with the aim of constraining the source characteristics and melting dynamics in this intraplate setting. These basalts have moderate-to-low silica (45.2 to 49.0 wt%), high Fe_2O_3T (10.0 to 12.2 wt%), and alkali ($Na_2O + K_2O$, 4.27 to 7.38 wt%) contents with ocean-island basalt (OIB) -like trace-element patterns and moderately depleted to slightly enriched Sr–Nd–Pb–Hf isotopes ($^{87}Sr/^{86}Sr$ = 0.703924–0.705176, $^{143}Nd/^{144}Nd$ = 0.512540–0.512861, $^{206}Pb/^{204}Pb$ = 17.2752–17.9180, $^{207}Pb/^{204}Pb$ = 15.4860–15.7383, $^{208}Pb/^{204}Pb$ = 37.6995–38.3599, and $^{176}Hf/^{177}Hf$ = 0.282852–0.282999). The major elements (e.g., high Fe/Mn, low CaO) and olivine chemistry (e.g., high Ni, Zn/Fe, and low Mn/Zn) favor derivation from a silica-deficient pyroxenite-bearing source, while the trace-element and isotope systematics suggest the involvement of recycled components including oceanic slab and sediment (both terrigenous and pelagic). A grid search with a thermodynamic melting model using incompatible trace elements was carried out to impose quantitative constraints on the mantle source. The modeling results show that the source of the Liangcheng basalt contains 80% primitive mantle peridotite and 20% silica-deficient pyroxenite. This exercise and geobarometric calculation using major elements suggest that melting occurs at a potential temperature of 1380 °C underneath a thinned continental lithosphere with a basal pressure of ~2GPa, consistent with the source characteristics and melting conditions estimated for many other volcanic fields in the vast Central-East Asia magmatic province. By combining these results with the regional geology and tectonic history, we can suggest that these basalts were formed by decompression melting owing to mantle convection driven by lithospheric thickness variations (edge-driven convection). We suggest that such a melting scenario is ubiquitous beneath Central-East Asia and may have played a vital role in the formation of widespread intraplate continental alkaline basalts.

1. Introduction

Intraplate volcanism distributed far from plate boundaries is important for understanding the geodynamic processes of Earth's mantle (King and Ritsema, 2000; Sobolev et al., 2005; Hoernle et al., 2006; Conrad et al., 2011; Ballmer et al., 2013; Wang et al., 2015). While high-volume (>10^5 km^3) magmatism is usually fed by mantle plumes (Bryan and Ernst, 2008), some small-volume diffusive magmatism shows no obvious connection with plate-boundary processes or mantle plumes (McGee and Smith, 2016). The origin of this intraplate volcanism remains unclear. The proposed models include: 1) splash plume triggered by cold downwelling material (Davies and Bunge, 2006); 2) passive upwelling caused by lithospheric thinning or rifting (Hoernle et al., 2006); 3) shear-driven upwelling related to relative motion between the lithosphere and asthenosphere (Conrad et al., 2011); 4) plate subduction-induced mantle upwelling (Kuritani et al., 2011); 5) edge-driven convection due to steps in lithospheric structure/thickness combined with plate movement (King and Ritsema, 2000).

* Corresponding author.
E-mail address: suyuping99@126.com (Y.-P. Su).

https://doi.org/10.1016/j.chemgeo.2023.121537
Received 3 March 2023; Received in revised form 5 May 2023; Accepted 6 May 2023
Available online 9 May 2023

The Central-East Asia continent became a coherent landmass after a series of Phanerozoic subduction and/or collision episodes, and it has witnessed widespread basaltic magmatism during the Cenozoic (Fig. 1A). P-wave tomography has revealed a stagnant subducted (Paleo-) Pacific plate in the mantle transition zone (Huang and Zhao, 2006), and the mantle domain above the plate is called the Big Mantle Wedge (BMW) (Zhao et al., 2004). Cenozoic basalts within the structure of the BMW span a wide composition range from extremely silica-deficient nephelinite to silica-excess quartz tholeiite (Xu et al., 2018). Lithological heterogeneous mantle sources containing garnet pyroxenite, eclogite, carbonated eclogite, and carbonated peridotite have been introduced to explain compositional variations (Liu et al., 2008a; Zeng et al., 2010, 2011, 2021; Huang et al., 2015; Li et al., 2017; Wang et al., 2017; He et al., 2019a; Yu et al., 2019; Xu et al., 2022; Zou et al., 2022). The melting of such lithological heterogeneities is generally interpreted to be related to the stagnant (Paleo-) Pacific slab in the mantle transition zone because of the spatial-temporal coincidence between the subducted slab and basalts (Figs. 1A, B; Chen et al., 2017; Xu et al., 2018; Cai et al., 2022), with some exceptions in which the melting is driven by small-scale convection due to lithospheric thickness variations (Guo et al., 2020; Sun et al., 2020; Xu et al., 2022). Cenozoic basalts beyond the BMW display geochemical compositions similar to their counterparts, and lithological heterogeneities have also been inferred from the source (He et al., 2019b; Pang et al., 2019; Sheldrick et al., 2020a; Zhang et al., 2021; Liu et al., 2022). However, unlike those within the BMW, basalts beyond the BMW are spatiotemporally far from any active margins (converge or disperse) (Windley et al., 2010; Xiao et al., 2015) and their melting mechanism remains hotly debated. Existing explanations include: 1) localized asthenospheric upwelling owing to lithospheric rifting or delamination (Barry et al., 2003; Hunt et al., 2012); 2) large-scale convection related to mantle plume (Johnson et al., 2005); 3) direct mantle melting triggered by coeval subduction/convergent processes, that is, subduction of the Pacific plate and/or India-Eurasia collision (Li et al., 2018; Chen and Faccenda, 2019). The above debates are largely owing to the lack of constraints on the thermal-chemical conditions of the lithologically heterogeneous mantle source, which are crucial for understanding the origin and melting mechanism of these intracontinental basalts.

Herein, we chose to study the Liangcheng basalts, which are far from the front edge of the stagnant Pacific slab (> 500 km) (Fig. 1B), to explore the mantle source characteristics and melting mechanisms of continental intraplate basalts. We present an integrated study on mineral chemistry, whole-rock geochemistry, Sr–Nd–Pb–Hf isotope compositions, and thermodynamic modeling to constrain their source characteristics and melting conditions. Our study reveals that these basalts originate from a silica-deficient pyroxenite-bearing mantle source with a low final melting pressure (~2 GPa) that corresponds to a thin lithosphere (< 70 km), which is consistent with most alkaline basalts in the studied and nearby regions. Our results, together with published geochemical data, geophysical observations, and regional geological history, suggest that decompression melting due to mantle convection driven by lithospheric thickness variations (edge-driven convection) may have played an important role in the formation of the Liangcheng basalts as well as many other Cenozoic intracontinental alkaline basalts across Central-East Asia.

2. Geological background and sample description

The Central-East Asia continent is composed of three cratons, including the Siberian Craton in the north, the North China Craton (NCC) in the middle, and the South China Craton in the south (Fig. 1A). Their assembly is marked by three major tectonic events, including the closure of the Paleo-Tethys Ocean between the South China Craton and the NCC before 200 Ma (Wu et al., 2009), the closure of the Paleo-Asian Ocean along the Solonker suture zone at 260–230 Ma (Wan et al., 2018; Jing et al., 2022), and the closure of the Mongol-Okhotsk Ocean along the Mongol-Okhotsk suture zone at 155–120 Ma (Kravchinsky et al., 2002; Van der Voo et al., 2015). After these tectonic events, the three cratons were bounded by two complex orogenic belts, namely the Central Asia Orogenic Belt between the NCC and the Siberia Craton and the Qinling-Dabie-Sulu Ultra-High Pressure Orogenic Belt between the NCC and the South China Craton (Fig. 1A).

The subduction of the (Paleo-) Pacific slab that started at ~180 Ma has led to the development of N-NE trending faulting and rifting systems, vast magmatism, and large-scale graben basins, as well as the formation of the North-South gravity lineament (NSGL) in East Asia (Ma and Xu, 2021 and references therein). Cenozoic basaltic magmatism in East Asia mainly occurred along the N-NE trending deep major faults (e.g., the Tan-Lu fault in the eastern NCC and Yilan-Yitong and Fushun-Mishan faults in NE China, Fig. 1A) or around the graben basins (e.g., Songliao Basin, Fig. 1A). In contrast, Central Asia (areas west of the NSGL) remains an intracontinental setting since the closure of the Mongol-Okhotsk Ocean during the Late Mesozoic to Early Cretaceous (Van der Voo et al., 2015; Sheldrick et al., 2020b) and is now away from the western leading edge of the Pacific slab, as revealed by the P-wave images (Huang and Zhao, 2006). The lithospheric thickness of Central Asia shows significant variations, as illustrated by geophysical observations and Mesozoic-Cenozoic basalt-born mantle xenoliths (Ionov, 2002; Chen et al., 2009a; Dai et al., 2020). The ancient blocks (Ordos, Gobi, and Siberia) are generally thick (> 200 km), whereas the segments between these ancient blocks commonly have a thin lithosphere, and Cenozoic basaltic magmatism is preferentially spread in regions with thin lithosphere (Fig. 1A).

The Liangcheng volcanic field belongs to the western part of NCC and locates at the joint of the Yinchuan-Hetao basin and the Shaanxi-Shanxi rift system (Fig. 1A) and has a wide distribution area of 1500 km^2 (Li and Li, 2003). It is underlain by thin (<100 km) and fertile lithospheric mantle, as evidenced by garnet-free lherzolite xenoliths in Cenozoic basalts (Zhang et al., 2012; Zhao et al., 2021) and seismic tomography (Chen et al., 2009a; Huang et al., 2009). Lithospheric thinning was proposed to have occurred at some point during the Early Cretaceous and Cenozoic, based on the compositional variation of regional basalts (Guo et al., 2014). The Neogene basalts are interbedded with several layers of sedimentary rocks (coal, mudstone, sandstone, and volcanic breccia), and unconformably underlain by the Archean TTGs and Jurassic-Cretaceous sandstone, shale, and tuff breccia, and overlain by Quaternary loess and sandstone (Fig. 2). These basalts occur either as volcanic cones or as lava flows with typical columnar jointing (Fig. S1) and the thickness of volcanic strata is basically >200 m and can up to 300 m in the southeast of the volcanic field. Whole-rock K–Ar dating of this volcanic field yields ages ranging from Oligocene to Miocene (24–15 Ma; Li and Li, 2003).

Thirty samples from 13 volcanic cones and three lava flow fields were collected, and only fresh samples without mineral cumulates were selected to be analyzed to obtain geochemical data. These rocks show a dark-grey colour with a massive structure and aphyric or porphyritic texture. The phenocrysts are dominated by olivine, with minor clinopyroxene. Olivine phenocrysts are euhedral to subhedral with embayed absorption shapes and vary in size from 0.5 mm to 2 mm, with a total amount of 5 vol%. Cracks developed, but no deformation structures were observed in the olivine grains (Fig. S1). Clinopyroxenes are anhedral and irregular in shape with a size of 0.5–1 mm and 1 vol% in volume (Fig. S1). The groundmass consists of olivine, clinopyroxene, plagioclase, Fe–Ti oxide microcrystals, and glass. No obvious petrographic evidence of magma mixing or mingling (e.g., complex zoning) was observed in these samples.

3. Analytical methods

3.1. In-situ mineral chemistry analyses

In-situ mineral (olivine, clinopyroxene, and feldspar) major-element

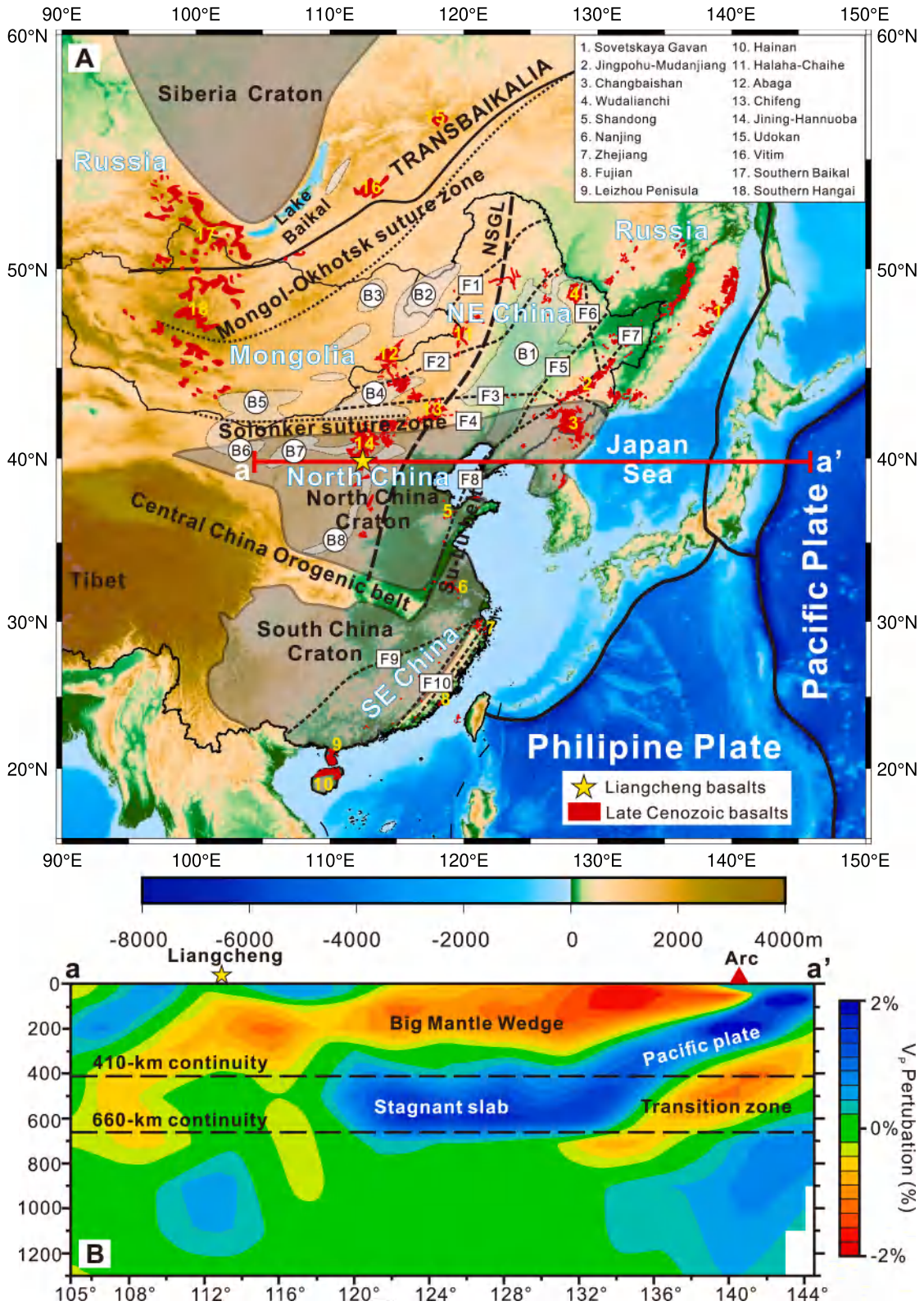

Fig. 1. (A) Topography map of Central-East Asia and distribution of late Cenozoic intraplate volcanic province; the distribution patterns of major faults, basins, and magmatism are according to Wang et al. (2015), He et al. (2019b) and Yu et al. (2019). (B) Seismic tomography image of the deeply subducted Pacific slab and structure of big mantle wedge (after Huang and Zhao, 2006). F1, Xinlin-Xiguitu fault; F2, Hegenshan-Heihe fault; F3, Solonker-Xar Moron-Changchun-Yanji suture; F4, Chifeng-Kaiyuan fault; F5, Yitong-Yilan fault; F6, Jiamusi fault; F7, Dunhua-Mishan fault; F8, Tan-Lu fault; F9, Jiang-Shao fault; F10, Songxi-Changting, Zhenghe-Dapu, and Changle-Nan'ao faults. B1, Songliao basin; B2, Hailarr basin; B3, Tamsag basin; B4, Erlian basin; B5, East Gobi basin; B6, Yin'gen basin; B7, Yinchuan-Hetao basin; B8, Shaanxi-Shanxi rift system.

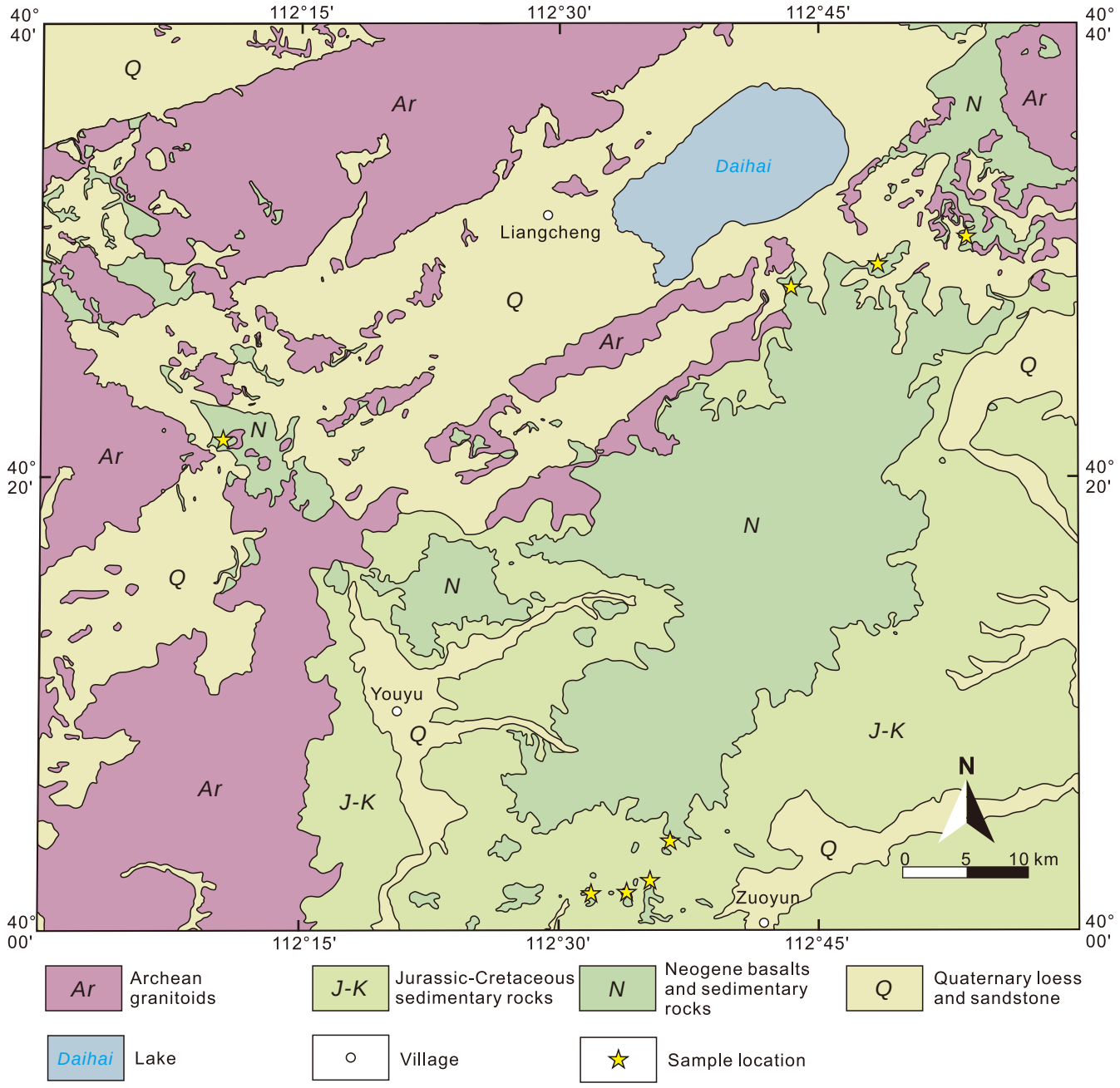

Fig. 2. Regional geological map of the Liangcheng volcanic field.

compositions were determined on carbon-coated polished sections using JXA-8100 electron microprobe at the Key Laboratory of Submarine Geosciences, Second Institute of Oceanography, Ministry of Natural Administration. The analyses were performed with an accelerating voltage of 15 kV, a 20 nA current, and beam diameters of 1–5 μm. Data were corrected using a modified ZAF (atomic number, absorption, fluorescence) correction procedure. Calibration standards were olivine (Mg), rutile (Ti), pyrope (Al), Cr_2O_3 (Cr), hematite (Fe), Mn_2O_3 (Mn), diopside (Si, Ca), jadeite (Na), and NiO (Ni). Peak counting times were 20 s and background counting times were 10 s on each side of the peaks. Internal standards (SPI olivine and diopside) were analyzed as unknown before the analyses, and the SPI olivine was also used as a secondary standard to check the olivine data accuracy. Analysis precision for measured contents >10% and > 0.5% are generally better than 1% and 5%, respectively, and for elements with contents <0.5 wt%, the precision may be less than 10%. The poor accuracy for elements with low concentrations is attributed to the instrument's precision and inappropriate experimental conditions (low electric current and/or short signal acquisition time) (Lambart et al., 2022). In-situ trace-element analysis for the olivine grains was conducted using a 193 nm RESOlution S-155 laser-ablation system coupled to a Thermo iCAP RQ inductively coupled plasma mass spectrometer (LA-ICP-MS) at the State Key Laboratory of Geological Processes and Mineral Resources (GPMR), China University of Geosciences, Wuhan. The analyzed samples were ablated using a 40 μm spot size, 10 Hz repetition rate, and 4 J/cm^2 corresponding energy density. Helium gas (~400 ml/min) carrying the ablated sample aerosol was mixed with Argon gas (~800 ml/min) and a small amount of Nitrogen gas (~4 ml/min) as an additional diatomic gas to enhance sensitivity, before flowing into the ICP-MS. Repeated analyses of the USGS standards (BIR-1G, BHVO-2G, and BCR-2G) indicate precision and accuracy are both better than 10% for most analyzed elements. The measured trace elements were: Li, P, Ca, Sc, Ti, V, Cr, Mn, Co, Ni, and Zn.

The NIST glasses were used for correcting the signal drift. The isotope ^{29}Si was used as the internal standard in conjunction with the Si concentrations determined previously by EPMA. ICPMSDataCal software (Liu et al., 2010) was used for the off-line data selection, integration of background and analyte signals, time-drift correction, and quantitative calibration. Data for olivine, clinopyroxene, and feldspar can be found in Table S1.

3.2. Whole-rock geochemical analyses

Whole-rock major-element compositions were determined by the traditional X-ray fluorescence (XRF) method using a Shimadzu Sequential 1800 spectrometer at GPMR. The detailed procedures were described by Ma et al. (2012). According to the measured values of standard (GBW07105), the analytical uncertainties for most elements are generally less than 5%. Bulk rock trace-element compositions were acquired using an Agilent 7700e ICP-MS after acid digestion of the samples in high-pressure Teflon bombs at Wuhan SampleSolution Analytical Technology Co., Ltd., (WSSAT). Sample powder (200 mesh) was placed in an oven at 105 °C for drying of 12 h. Then, 50 mg sample powder was weighed and placed in a Teflon bomb, and 1.5 ml of HNO_3 and 1.5 ml of HF were added to the bomb, which was sealed in a steel jacket and heated to 190 °C in the oven for 48 h to completely dissolve the sample. After cooling, the Teflon bomb was opened and placed on a hotplate at 140 °C and evaporated to incipient dryness, and the 1 ml HNO_3 was added and evaporated to a second round of dryness. The resultant salt was redissolved by 1 ml of HNO_3, 1 ml of Milli-Q water, and 1 ml internal standard solution of 1 ppm In, and the Teflon bomb was resealed and placed in the oven at 190 °C for >12 h. The final solution was diluted to 100 g with a mixture of 2% HNO_3 for ICP-MS analysis. Analyses of four international standards (AGV-2, BHVO-2, BCR-2, and RGM-2) indicate that the analytical uncertainties for most trace elements are generally less than 5%. The detailed sample digestion procedure and the analytical precision and accuracy during ICP-MS analyses were the same as those described in Liu et al. (2008b). Whole-rock major and trace element data for samples and standards are listed in Table S2.

3.3. Sr–Nd–Pb–Hf isotopic analyses

Nine samples were selected for whole-rock Sr–Nd–Pb–Hf isotope analysis at the WSSAT. For the Sr–Nd isotopic analysis, approximately 200 mg of the sample powder was completely dissolved in HF-$HClO_4$ at 200 °C for one week. Sr and Nd were separated using conventional ion-exchange columns, and Nd fractions were further separated using HDEHP columns. The procedural blanks were 200 pg for Sr and 30 pg for Nd. The measured $^{87}Sr/^{86}Sr$ and $^{143}Nd/^{144}Nd$ ratios were normalized to $^{88}Sr/^{86}Sr = 8.3752$ and $^{146}Nd/^{144}Nd = 0.7219$, respectively. The measured values for the NBS987 standard yielded $^{87}Sr/^{86}Sr = 0.710243 \pm 0.000010$ (2SE, $n = 4$), and the GSB 04-3258-2015 standard yielded $^{143}Nd/^{144}Nd = 0.512441 \pm 0.000006$ (2SE, n = 4). The USGS reference materials BCR-2 and RGM-2 gave results of 0.704999 ± 0.000007 (2SE, $n = 1$) and 0.704143 ± 0.000008 (2SE, n = 1), respectively, for $^{87}Sr/^{86}Sr$ and 0.512640 ± 0.000006 (2SE, n = 1) and 0.512793 ± 0.000006 (2SE, n = 1), respectively, for $^{143}Nd/^{144}Nd$. These values are identical, within error of 0.03% of their recommended values (Thirlwall, 1991; Weis et al., 2006; Li et al., 2012, 2016a).

For Pb isotopic determination, the whole rock powder was dissolved in Teflon vials with purified HF + HNO_3 at 190 °C for >24 h and then separated using anion-exchange columns with diluted HBr and HCl as eluents. The procedural blank for Pb was 50 pg. Isotopic ratios were also determined using the Neptune Plus MC-ICP-MS. Repeated analyses of Pb isotopes for standard NBS981 yielded $^{208}Pb/^{204}Pb = 36.727 \pm 0.002$, $^{207}Pb/^{204}Pb = 15.500 \pm 0.001$, and $^{206}Pb/^{204}Pb = 16.942 \pm 0.001$ (2SE, $n = 3$). For the in-house Alfa Pb standard the values were $^{208}Pb/^{204}Pb = 37.851 \pm 0.002$, $^{207}Pb/^{204}Pb = 15.597 \pm 0.001$, and $^{206}Pb/^{204}Pb = 17.917 \pm 0.001$ (2SE, n = 3). The USGS reference materials BCR-2 yielded results of $^{208}Pb/^{204}Pb = 38.741 \pm 0.001$, $^{207}Pb/^{204}Pb = 15.627 \pm 0.000$, and $^{206}Pb/^{204}Pb = 18.758 \pm 0.001$ (2SE, $n = 1$), and the RGM-2 yielded results of $^{208}Pb/^{204}Pb = 38.647 \pm 0.002$, $^{207}Pb/^{204}Pb = 15.621 \pm 0.001$, and $^{206}Pb/^{204}Pb = 18.933 \pm 0.001$ (2SE, n = 1). The measured standards and references were identical within the error of the recommended values (Baker et al., 2004; Weis et al., 2006).

For Hf isotopic analysis, approximately 200 mg of the powder was digested in Teflon bombs with a mixture of concentrated HNO_3 + HF and dried on a hot plate. This was followed by the addition of concentrated HNO_3, HF, and $HClO_4$ sealed in bombs and kept in an oven at 190 °C. After cooling, the Teflon bomb was opened, and 1 ml HNO_3 was added and evaporated to dryness. A modified ion-exchange single-column LN-Spec resin was used for Hf separation. The procedural blank for Hf was 50 pg. Mass discrimination correction was performed via internal normalization to a $^{179}Hf/^{177}Hf$ ratio of 0.7325. The in-house AlfaHf standard measured during analysis gave an average $^{176}Hf/^{177}Hf$ ratio of 0.282224 ± 0.000006 (2SE, $n = 5$), and the reference materials BCR-2 and RGM-2 yielded $^{176}Hf/^{177}Hf$ ratios of 0.282855 ± 0.000007 (2SE, $n = 1$) and 0.283010 ± 0.000007 (2SE, n = 1), respectively, which are within the range of the recommended values (Weis et al., 2007; Chen et al., 2013). The whole-rock Sr–Nd–Pb–Hf isotopic data are shown in Table 1.

4. Results

The olivine grains have forsterite contents [Fo = 100*Mg/(Mg + Fe)] varying from 64.7 to 86.5 (Fig. S2), and most of them are in equilibrium with the whole rock, assuming the Fe–Mg partition coefficient ($K_D = 0.30 \pm 0.03$) between olivine and melt (Fig. S2; Roeder and Emslie, 1970). Their CaO contents (0.1–0.26 wt%, Table S1) were slightly higher than those of typical mantle olivine (CaO < 0.1 wt%; Foley et al., 2013), together with the euhedral and subhedral crystal shapes, suggesting that they were precipitated from magmas instead of being xenocrysts. In addition, they have high Ni (0.07–0.40 wt%, corresponding to 534–3104 ppm) and Zn (99–244 ppm) and varied Mn (0.10–0.26 wt %, corresponding to 767–1990 ppm) concentrations with 100*Mn/Fe ratios of 0.53–1.85 and 10,000*Zn/Fe ratios of 9.15–17.6. It should be noted that except for the Ni concentrations, other trace elements (e.g., Ca, Mn) of olivine presented here are acquired through LA-ICP-MS as these elements have concentrations that are too low to have acceptable precision by EPMA (uncertainty >10%) when measured by routine analysis (see section 3), which is also suggested by the poor correlations between data from EPMA and LA-ICP-MS (Fig. S3). Clinopyroxenes are mainly diopside ($Wo_{36-48}En_{27-39}Fs_{6-18}CaTs_{8-21}$) (Fig. S2) and have TiO_2 contents of 0.20–3.21 wt%, Al_2O_3 contents of 3.41–9.89 wt%, and $Mg^{\#}$ values of 47.7–70.8. The compositions of feldspar vary from andesine to labradorite (An_{38-65}) (Fig. S2).

The Liangcheng basalts have SiO_2 contents of 45.2 to 49.0 wt%, and high contents of alkali elements ($K_2O + Na_2O$) (4.27–7.38 wt%) and belong to the alkaline series (Fig. 3A). These rocks display various MgO contents (5.69–9.54 wt%), low CaO (6.70–9.36 wt%) and MnO (0.12–0.16 wt%), and high Fe_2O_3T (10.1–12.2 wt%) contents with correspondingly high Fe/Mn ratios (59.2–81.1). The TiO_2 (1.77–2.43 wt %), Fe_2O_3T, and MnO contents are nearly invariant with decreasing MgO contents. The CaO/Al_2O_3 ratios positively correlate with the MgO contents for samples with MgO < 8 wt%, but show no obvious correlation for those with MgO ≥ 8 wt% (Fig. 3B). The Liangcheng basalts display ocean-island basalt (OIB) -type trace-element patterns, which are, enriched in large ion lithophile elements (LILEs) and light rare earth elements (LREEs) with positive anomalies in Nb, Ta, Sr, Ba, and negative anomalies in Th, and Pb (Fig. 4). These samples show radiogenic Sr isotopes ($^{87}Sr/^{86}Sr = 0.703924–0.705688$) and moderately depleted to slightly enriched Nd–Hf isotopes ($^{143}Nd/^{144}Nd = 0.512539–0.512861$, $^{176}Hf/^{177}Hf = 0.282824–0.282999$), with positive correlations in the

Table 1
Whole-rock Sr-Nd-Pb-Hf isotopes for the Liangcheng basalts.

	$^{206}Pb/^{204}Pb$	2σ	$^{207}Pb/^{204}Pb$	2σ	$^{208}Pb/^{204}Pb$	2σ	$^{87}Sr/^{86}Sr$	2σ	$^{143}Nd/^{144}Nd$	2σ	ε_{Nd}	$^{176}Hf/^{177}Hf$	2σ	ε_{Hf}
20XJY-2	17.7073	0.0030	15.5631	0.0012	37.8448	0.0014	0.704359	0.000009	0.512705	0.0000053	1.3	0.282960	0.000010	6.6
20QJY-3	17.8041	0.0023	15.7383	0.0009	38.1346	0.0011	0.704605	0.000009	0.512681	0.0000068	0.8	0.282935	0.000009	5.8
20SDH-1	17.8147	0.0016	15.5487	0.0006	37.9705	0.0007	0.704723	0.000010	0.512861	0.0000061	4.4	0.282997	0.000006	8.0
20FSS-3	17.7325	0.0018	15.5341	0.0007	37.9025	0.0008	0.704595	0.000010	0.512792	0.0000058	3.0	0.282980	0.000007	7.4
20QLZ-B9	17.9158	0.0032	15.6631	0.0013	38.3599	0.0015	0.703924	0.000010	0.512836	0.0000048	3.9	0.282999	0.000007	8.0
20MXSYZ-1	17.2752	0.0024	15.5215	0.0010	37.8097	0.0010	0.704601	0.000010	0.512670	0.0000057	0.6	0.282864	0.000016	3.3
20MPZ-B1	17.5359	0.0015	15.5129	0.0006	37.6995	0.0007	0.705176	0.000008	0.512540	0.0000042	−1.9	0.282852	0.000009	2.8
20GQZ-1	17.8530	0.0014	15.5050	0.0005	37.9452	0.0006	0.705688	0.000009	0.512539	0.0000071	−1.9	0.282824	0.000007	1.8
20QLZ-B6	17.5990	0.0014	15.4860	0.0004	37.7292	0.0005	0.704236	0.000009	0.512794	0.0000073	3.0	0.282982	0.000008	7.4

$\varepsilon_{Nd} = [(^{143}Nd/^{144}Nd)_{sample}/(^{143}Nd/^{144}Nd)_{CHUR} - 1] \times 10^4$; where $(^{143}Nd/^{144}Nd)_{CHUR} = 0.51263$ (Bouvier et al., 2008).
$\varepsilon_{Hf} = [(^{176}Hf/^{177}Hf)_{sample}/(^{176}Hf/^{177}Hf)_{CHUR} - 1] \times 10^4$; where $(^{176}Hf/^{177}Hf)_{CHUR} = 0.282785$ (Bouvier et al., 2008).

References
Bouvier A., Vervoort J. D., Patchett P. J., 2008. The Lu–Hf and Sm–Nd isotopic composition of CHUR: Constraints from unequilibrated chondrites and implications for the bulk composition of terrestrial planets. Earth Planet. Sci. Lett. 273, 48–57.

plot of $^{143}Nd/^{144}Nd$ vs. $^{176}Hf/^{177}Hf$ (Figs. 5A, B). They are distinct from Pacific MORB owing to their higher $^{207}Pb/^{204}Pb$ and $^{208}Pb/^{204}Pb$ compared to the standard $^{206}Pb/^{204}Pb$ and show similarities with Indian MORB (Figs. 5C, D).

5. Discussion

5.1. Alteration, contamination, and differentiation

The post-magmatic alteration effect on the compositions of the basalts is neglected because of the low LOI values (< 3 wt%, Table S2) and overall freshness in hand specimens and thin sections. This could be further assessed by the correlation between LILEs (e.g., Rb, Sr, Ba, and LREE) and high field strength elements (HFSEs) (e.g., Zr and Hf), as both group elements are incompatible during mantle partial melting or crystallization (Bédard, 2006), and positive correlations would be observed if they are only controlled by magmatic processes (Polat et al., 2002). In contrast, if the alteration were significant, the correlation would be disturbed because LILEs can be mobilized during alteration while HFSEs tend to remain immobile under similar conditions (Polat et al., 2002). The good correlation between the LILEs and HFSEs in the Liangcheng basalts suggests that the alteration was insignificant (Fig. S4), except for one sample (20GQZ-1) that may have suffered slightly alteration according to its petrological features (altered minerals and groundmass), the highest LOI (2.63 wt%) among collected basalts, and elevated Rb and Pb concentrations (Fig. S4).

Crustal contamination is also negligible because most of the studied basalts have trace element patterns similar to the enriched mantle-type OIB with remarkably positive Nb–Ta anomalies, negative Th and Pb anomalies, high Nb/U, Ce/Pb, and low Zr/Nb ratios, in contrast with the continental crust (Figs. 4, S5, Table S2; Rudnick and Gao, 2014). The lack of correlations between isotopes (Sr, Nd, Hf) and MgO is also inconsistent with crustal contamination (Fig. S5), as the continental crust is characterized by low MgO content, radiogenic Sr and unradiogenic Nd–Hf isotopic compositions (Liu et al., 2004).

The positive correlation between CaO and MgO contents implies the fractionation of clinopyroxene (Table S2). However, CaO variations may also be affected by source heterogeneity. Positive correlations between CaO and radio-isotopes ($^{143}Nd/^{144}Nd$, $^{176}Hf/^{177}Hf$) are observed for basalts with high MgO contents (≥ 8 wt%), suggesting that the variation of CaO for these basalts may be affected by mantle source heterogeneity rather than magma differentiation (Fig. S6). Except for CaO contents, CaO/Al_2O_3 ratios and Sc concentrations are primarily controlled by clinopyroxene; thus, their variations can be used to evaluate the effect of clinopyroxene fractionation. Positive trends exist among CaO/Al_2O_3, Sc, and MgO in the samples with MgO < 8 wt%, but no obvious correlations are presented in samples with MgO ≥ 8 wt%, indicating negligible clinopyroxene crystallization for high MgO samples (Figs. 3B, C). The generally positive correlation between Ni and MgO reflects olivine removal throughout magma differentiation because of the compatibility of Ni in olivine from the alkaline basalts (Fig. 3D). In addition, the absence of plagioclase phenocrysts and weak Eu anomalies (Eu/Eu* = 0.98–1.06, where $Eu/Eu^* = Eu_N/(Sm_N*Nd_N)^{0.5}$; N, chondrite normalized) suggests that the plagioclase fractionation is minor (Fig. 4, Table S2). The consistent TiO_2 and Fe_2O_3T with decreasing MgO also indicate insignificant fractionation of Fe–Ti oxides (Table S2). These results suggest that the high-MgO samples may have only experienced olivine fractionation. This conclusion is consistent with previous studies on regional Cenozoic basalts (Liu et al., 2008a; Xu et al., 2017). To minimize the effects of mineral fractionation, we chose rocks with MgO ≥ 8 wt% to constrain their source lithologies and melting conditions.

5.2. Source lithology

Mineral (especially olivine) compositions (Sobolev et al., 2005; Herzberg, 2011; Foley et al., 2013) and whole-rock geochemical

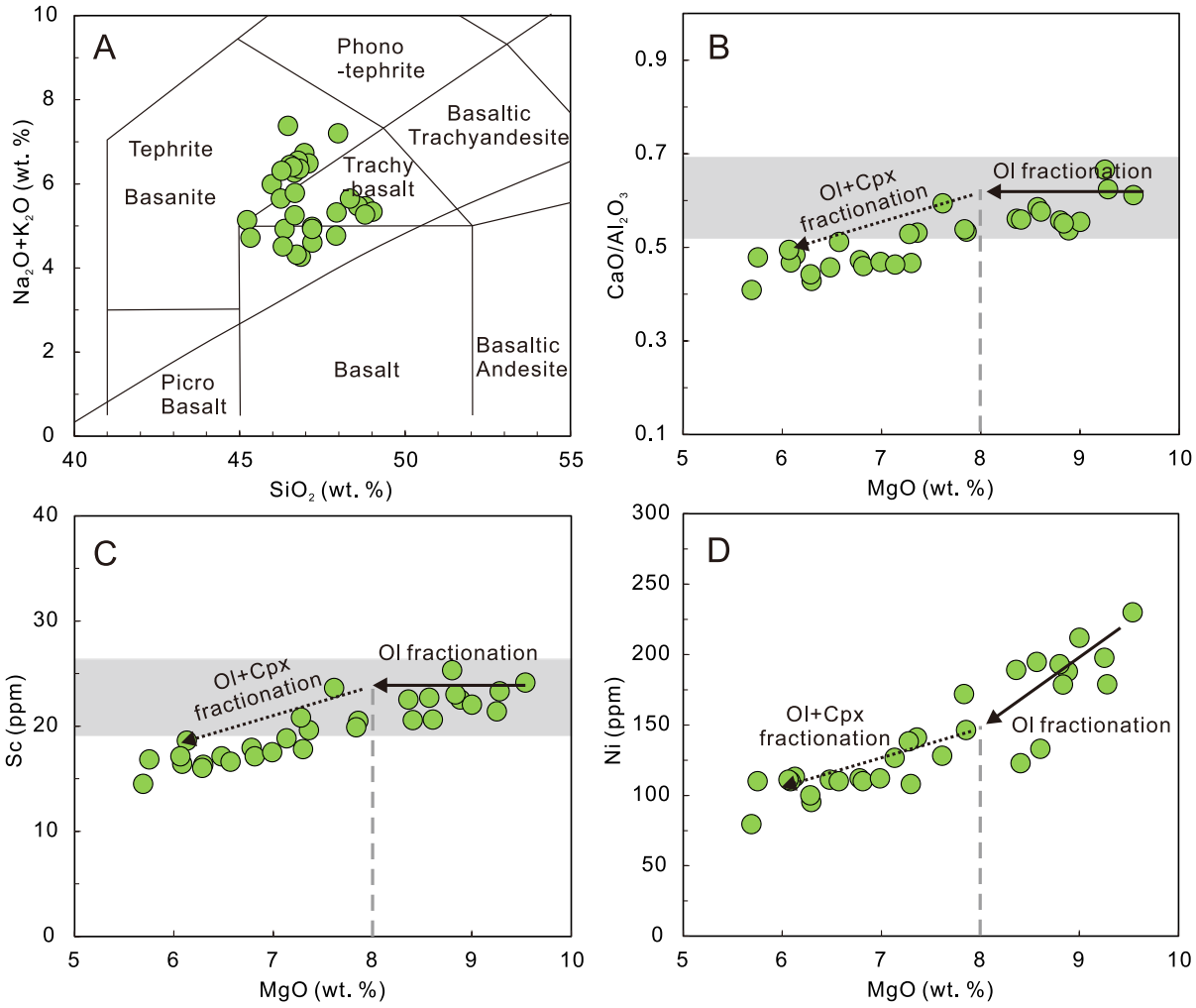

Fig. 3. (A) Total alkali ($Na_2O + K_2O$) vs. SiO_2 contents (Le Bas et al., 1986); CaO/Al_2O_3 ratios (B), Sc concentrations (C), and Ni concentrations vs. MgO contents (D).

contents (e.g., CaO contents, Herzberg, 2011) and ratios (Fe/Mn, Zn/Fe, FC3MS, FCKANTMS, Liu et al., 2008a; Le Roux et al., 2010; Yang and Zhou, 2013; Yang et al., 2019) have been proposed as useful tools to discriminate the source lithology of basalts. The olivine phenocrysts of the Liangcheng basalts display high Ni concentrations, and low Mn and Ca concentrations that are similar to olivine from typical pyroxenite-derived basalts, such as those from Koolau and Loihi, suggesting crystallization from pyroxenite melts (Figs. 6A, B, C; Sobolev et al., 2005; Herzberg, 2011; Foley et al., 2013; Shi et al., 2022). However, recent experimental studies showed that Ni and Mn partition coefficients between olivine and melt are related to pressure and temperature conditions, which may cause Ni enrichment and Mn depletion in melt derived from high-pressure melting of a peridotite source (Matzen et al., 2017). This weakness can be improved by using additional indexes such as transition elements and their ratios (Mn, Zn, Fe, Zn/Fe, Mn/Zn, and Mn/Fe; Howarth and Harris, 2017). The Zn/Fe, Mn/Zn, and Mn/Fe ratios for olivine grains of Fo > 80 from Liangcheng basalts straddle from the field of pyroxenite-peridotite mixed to pyroxenite source, suggesting a pyroxenite-bearing mantle source lithology (Figs. 6D, E, F). In addition, the whole-rock TiO_2 and MnO contents of Liangcheng basalts show little variation during magma evolution and thus can be used to discriminate the source lithology via comparison with experimental data (Table S2). The studied basalts are characterized by high TiO_2 contents and all fall into the field of pyroxenite (both silica-excess and silica-deficient) melts (Fig. 7A). Besides that, a whole-rock major composition-based indicator of FC3MS ($FeO/CaO\text{-}3MgO/SiO_2$) proposed by Yang and Zhou (2013) has been suggested as useful to discriminate the source lithology of basalt. Yang and Zhou (2013) compiled experimental and natural data of peridotite and pyroxenite melts and suggested that the upper limit of FC3MS value for peridotite melts is 0.65, and higher FC3MS value for peridotite melts can only be reached by substantial clinopyroxene fractionation (> 30%), which is unrealistic for the Liangcheng basalts with high MgO contents (≥ 8 wt%) because they only experienced olivine fractionation. Therefore, the high FC3MS values (0.49–0.77) of the Liangcheng basalts may suggest contributions from pyroxenite melts (Fig. 7B). In addition, the recently proposed parameter, FCKANTMS ($\ln(FeO/CaO)\text{-}0.08*\ln(K_2O/Al_2O_3)\text{-}0.052*\ln(TiO_2/Na_2O)\text{-}0.036*\ln(Na_2O/K_2O)*\ln(Na_2O/TiO_2)\text{-}0.062*(\ln(MgO/SiO_2))^3\text{–}0.641*(\ln(MgO/SiO_2))^2\text{–}1.871*\ln(MgO/SiO_2)\text{-}1.473$) is also a useful index in discriminating the source lithology of basalt, and olivine fractionation only causes limited variation (0–0.15) of this value (Yang et al., 2019). The Liangcheng basalts have much higher FCKANTMS (0.42–0.64) than those for peridotite melts (< 0.1) as shown in Figs. 7C, D, also indicating a major contribution from pyroxenite melting. The above evidence collectively suggests a pyroxenite-bearing mantle source lithology for the Liangcheng basalts.

Discriminating the nature of the pyroxenite is of great importance before we gain knowledge about the melting conditions because different types of pyroxenite may have various mineral modes, phase relations, and melting behavior (Lambart et al., 2016). The nature of pyroxenite could be identified using whole-rock compositions since different types of pyroxenites (silica-deficient and silica-excess) would

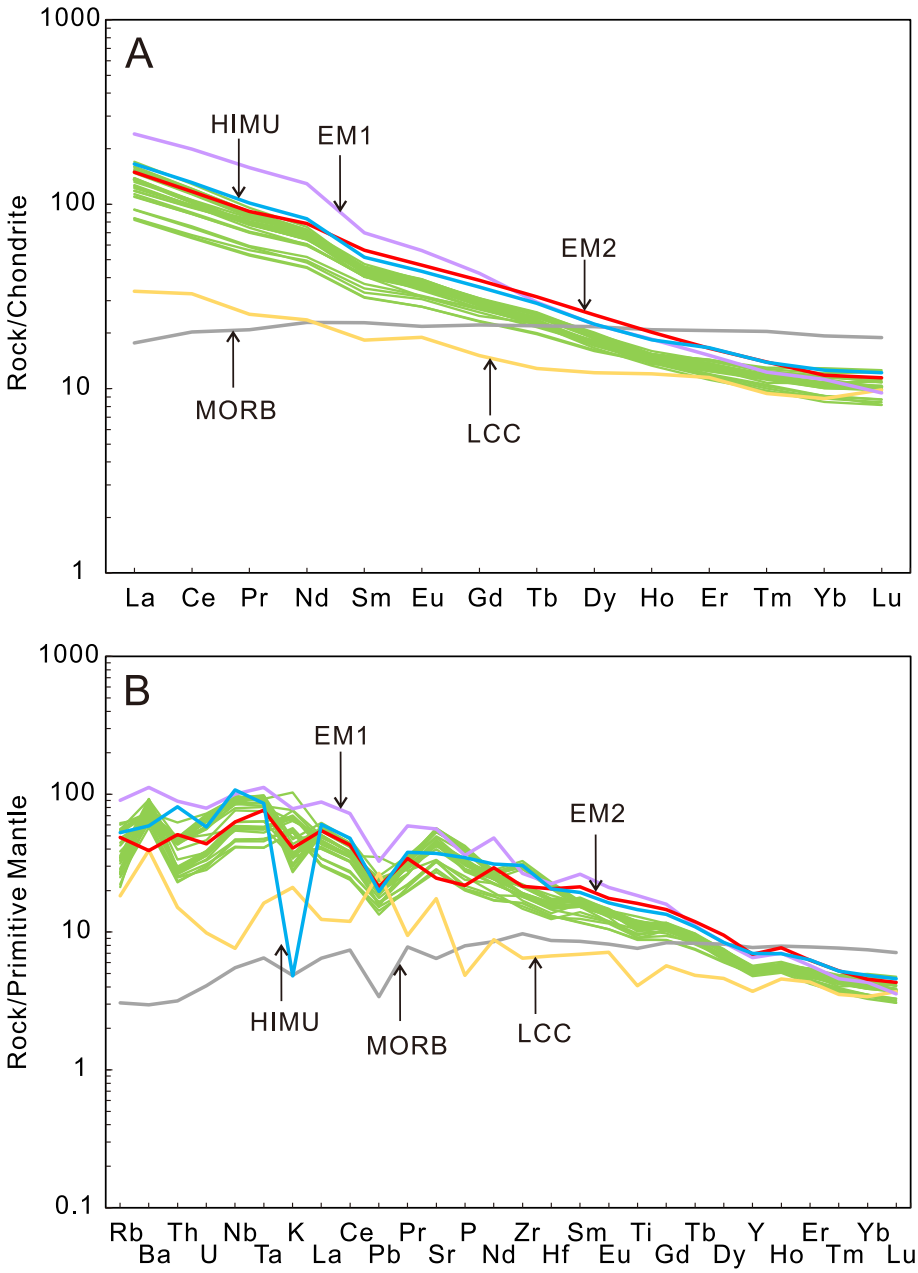

Fig. 4. (A) Chondrite-normalized REE patterns; (B) primitive mantle-normalized spider diagrams. Normalizing data for the chondrite and primitive mantle are from Sun and McDonough (1989) and McDonough and Sun (1995), respectively. The data source for the average MORB is from Gale et al. (2013), the average HIMU, EM1, and EM2 are from Kawabata et al. (2011), Willbold and Stracke (2006) and Workman et al. (2004), respectively, and the lower continental crust (LCC) is from Rudnick and Gao (2014).

generate melts with contrasting compositions (Lambart et al., 2013). Here, we adopted a pseudo-ternary sub-projection consisting of a whole array of major elements to provide insights into the nature of the pyroxenite in the source of the studied basalts (Fig. 8). It clearly shows that the Liangcheng basalts with high MgO contents ($\geq$ 8 wt%) are deficient in SiO_2 and similar to experimental melts of silica-deficient pyroxenite, and addition of olivine (to recover the primary melt composition) would not drive these basalts into fields of silica-excess pyroxenite melts. Although experiments proposed that reacted melts between MORB-eclogite (silica-excess pyroxenite) partial melts and fertile peridotite could generate basalts with low silica and high alkali that are similar to natural alkaline basalts (Mallik and Dasgupta, 2012), we suggest such a scenario is not the case for the Liangcheng basalts since these basalts exhibit much lower TiO_2 contents at similar MnO contents, indicating inconsistency with the reacted melts (Fig. 7A). As a consequence, we suggest that the pyroxenite in the source of the Liangcheng basalts is silica-deficient pyroxenite.

5.3. *Melting conditions of the pyroxenite-bearing asthenosphere*

Preferential melting of non-peridotite source lithology extracts latent heat from the ambient mantle and further facilitates the melting process, but suppresses the melting of the surrounding peridotite (Oliveira et al., 2021). Consequently, the mass contribution of such low-solidus lithology (e.g., pyroxenite) to the melt overweighs its proportion in the mantle (Lambart et al., 2016). The complicated chemical and thermal processes make it difficult to recover the melting condition based on the bulk major-element compositions of primary magma acquired by reverse methods for single-source lithology (e.g., the addition or removal of olivine, Lee et al., 2009; Herzberg, 2011). Herein, we employed a forward-modeling method based on whole-rock incompatible trace-element compositions using REEBOX PRO (Brown and Lesher, 2016) to explore the melting conditions and source characteristics.

REEBOX PRO is a software package that can simulate the adiabatic decompression melting of heterogeneous mantle sources containing anhydrous peridotite (lherzolite), hydrous peridotite (lherzolite),

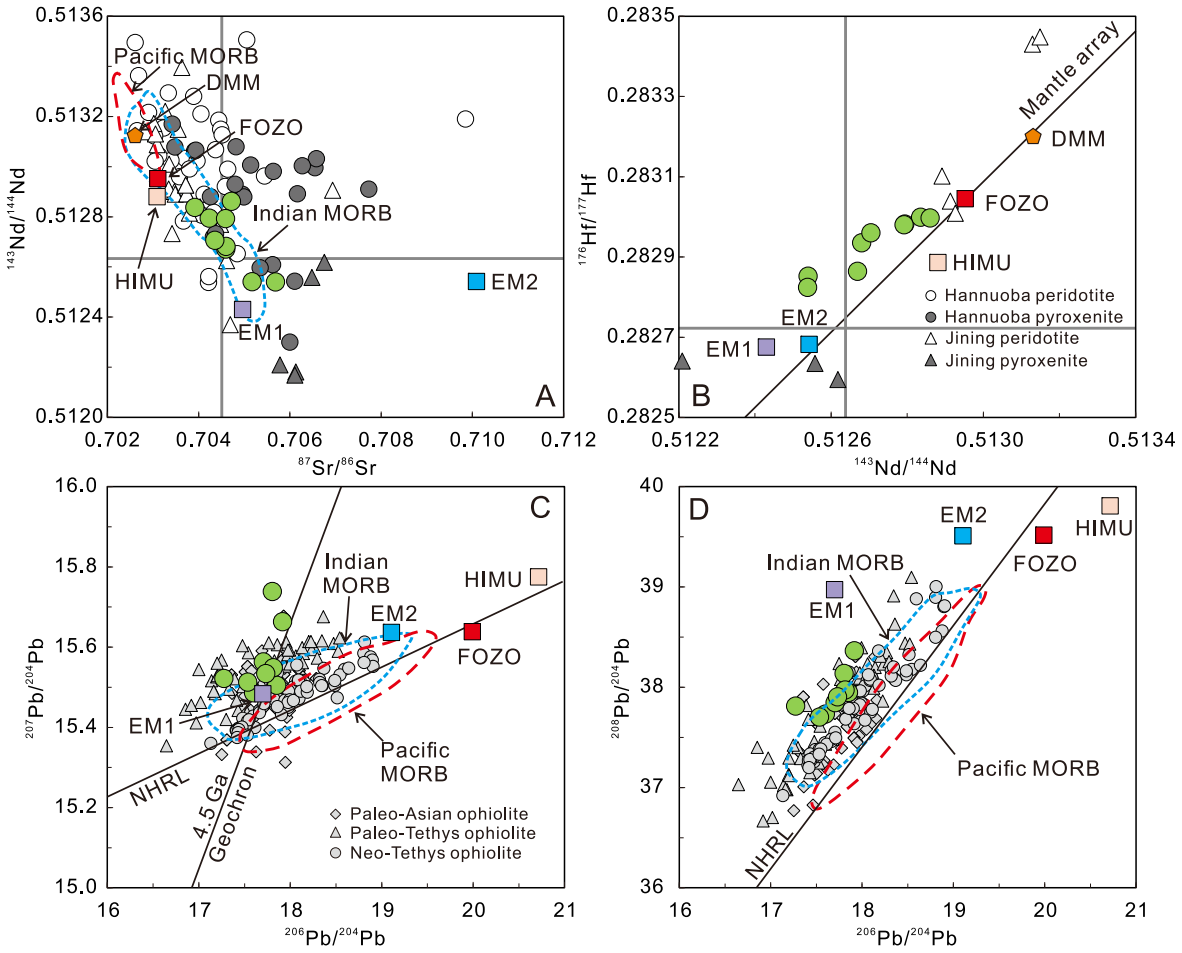

Fig. 5. Whole-rock (A) $^{143}Nd/^{144}Nd$ vs. $^{87}Sr/^{86}Sr$; (B) $^{176}Hf/^{177}Hf$ vs. $^{143}Nd/^{144}Nd$; (C) $^{207}Pb/^{204}Pb$ vs. $^{206}Pb/^{204}Pb$; (D) $^{208}Pb/^{204}Pb$ vs. $^{206}Pb/^{204}Pb$ diagrams. The areas for Indian MORB and Pacific MORB are taken from Xu and Zheng (2019), and data for FOZO (Cook-Austral), HIMU (St. Helena), EM1 (Pitcairn), and EM2 (Samoa) are from the GEOROC database (http://georoc.mpch-mainz.gwdg.de/georoc/). The average Sr, Nd, Pb, and Hf isotopic compositions for depleted-MORB mantle (DMM) are from Workman and Hart (2005) and references therein. The data of ophiolites from the Neo-Tethys Ocean, Paleo-Tethys Ocean, and Paleo-Asian Ocean are compiled in Liu et al. (2015c). The mantle xenoliths from Hannuoba and Jining are compiled in Zhao et al. (2021).

pyroxenite (three types: G2, MIX1G, and KG1 pyroxenite) and/or residual harzburgite (Brown and Lesher, 2016; Brown et al., 2020). The key model inputs include the mantle potential temperature, lithospheric thickness, trace element abundances, isotopic composition, and water content of the source rocks. Assuming that all specified lithologies are in thermal equilibrium rather than chemical equilibrium, the program uses thermodynamic and experimental constraints to quantify their polybaric productivities (dF/dP) at discrete decompression steps (per 0.01 GPa) between the deepest solidus and the base of the lithosphere. The mineral model parameterizations of the solidus are based on experimental constraints and thermodynamic modeling using Perple_X (Connolly, 1990, 2005). Using experimentally constrained mineral modes, melting modes, and either temperature-dependent or static mineral-melt partition coefficients, the model then calculates the compositions of instantaneous melts generated by the incremental batch melting of each lithology during each decompression step. For each lithology, instantaneous melts are mixed along the melting column to provide a "column-accumulated" melt composition at the top of the melting column. Finally, the bulk (aggregate) igneous crust thickness and composition are calculated by pooling all column-accumulated melts derived from all the lithologies (pooled melts) (Brown et al., 2020).

Before the modeling, we need to point out that the factor of CO_2 was not taken into account in the software, which may affect the results because the carbonated mantle source has been proposed to play an important role in forming the Cenozoic alkaline basalts in Central-East Asia (Zeng et al., 2010, 2021; Yang et al., 2012; Sakuyama et al., 2013; Huang et al., 2015; Li et al., 2017; Wang et al., 2017; Xu et al., 2018; He et al., 2019b; Cai et al., 2022; Zou et al., 2022). To explore whether CO_2 is involved in the mantle source of the Liangcheng basalts, we used a SiO_2 vs. CaO diagram for discrimination (Herzberg and Asimow, 2008, Fig. S7). The theory behind this method lies in the fact that CO_2-bearing basalts are usually characterized by much lower SiO_2 and higher CaO than CO_2-free basalts (Herzberg and Asimow, 2008). The results show that the Liangcheng basalts plot in the region of CO_2-free basalts, suggesting that the impact of CO_2 on the studied basalts was minor (Fig. S7). This inference is supported by evidence that the negative anomalies in Zr–Hf and Ti, which are typical features of CO_2-bearing basalts, are not observed in the studied samples (Zeng et al., 2010). Although we could not rule out the possibility that CO_2 had once been involved in the source region, for which case the melts gradually evolved from carbonatitic melt to carbonate silicate melt and eventually to alkaline basalts (Xu et al., 2020 and references therein), we suggest that in this situation the effect of CO_2 on the composition of the basalts has been strongly diluted and therefore has an insignificant influence on the final melt compositions.

After evaluating the CO_2 impact, we conducted our modeling using the REEBOX PRO software. Four main controlling factors were considered in the modeling: (1) mantle potential temperatures, (2) source water content, (3) source compositions (lithological proportions), and (4) final depths of melting (lithosphere-asthenosphere boundary). Grid

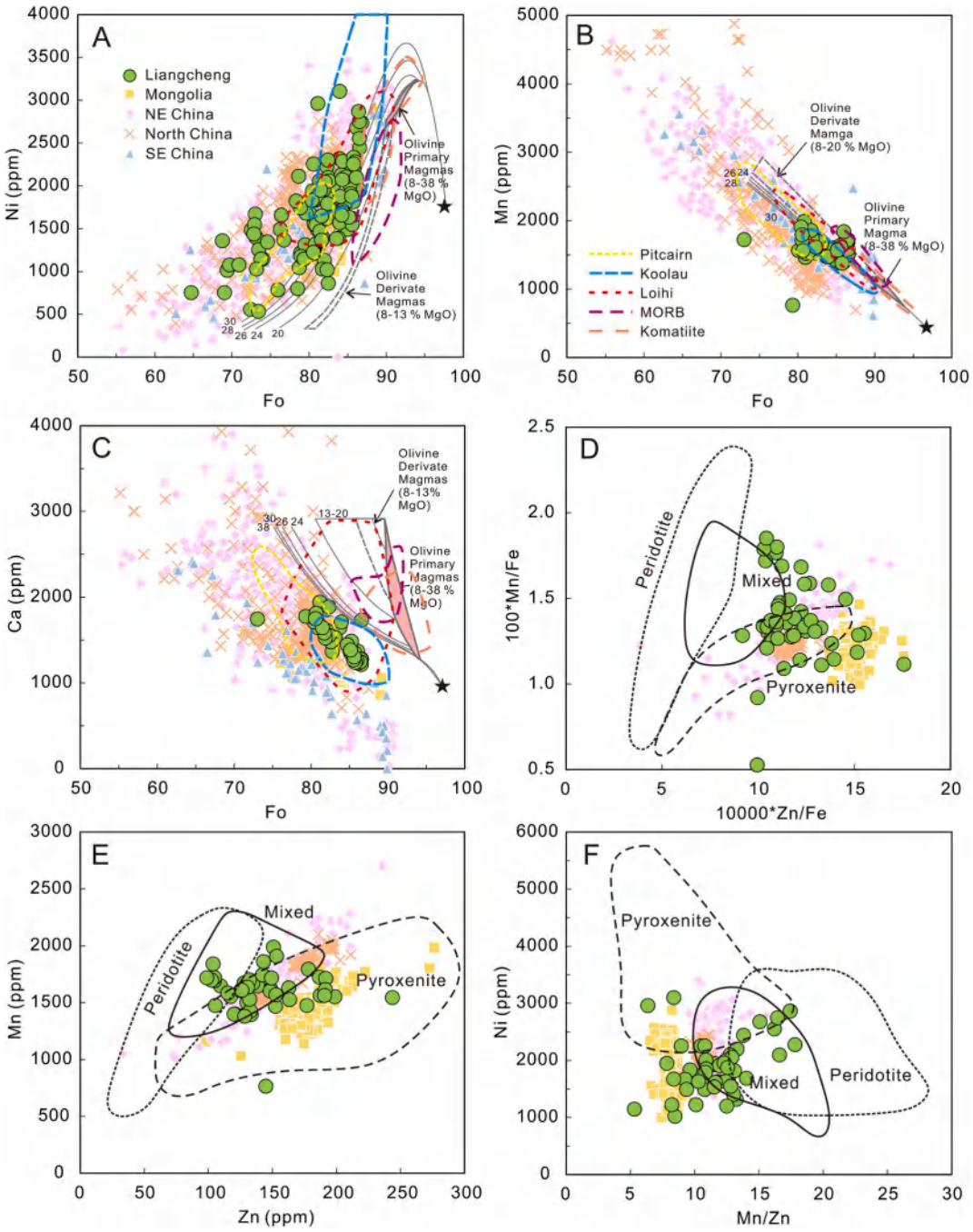

Fig. 6. Ni concentrations (A), Mn concentrations (B), and Ca concentrations (C) vs. Fo for olivine grains in the Liangcheng basalts; (D) 100*Mn/Fe vs. 10,000*Zn/Fe ratios, (E) Mn vs. Zn concentrations and (F) Ni concentrations vs. Mn/Zn ratios diagrams for Liangcheng olivine phenocrysts. Olivine Ni data plotted in (A) is from EPMA, while the Mn and Ca data plotted in (B) and (C) are acquired by LA-ICP-MS. The compositions of olivines crystallized from peridotite melts calculated by Herzberg (2011) are shown for comparison. The calculation was based on a fertile peridotite source with Ni of 1,964 ppm, Ca of 24,657 ppm, and Mn of 1,007 Mn. The calculated olivines are for both primary magmas and derivative magmas produced by olivine fractionation. The filled fields are for calculated olivines of the primary magmas. The other numbered lines and fields are for calculated olivines from derivative magmas with different MgO contents (Herzberg, 2011). Fields for olivines that have been interpreted to be derived from pyroxenite, peridotite, and pyroxenite-peridotite mixed source are from Howarth and Harris (2017) and references therein, and for olivine from Pitcairn, Koolau, Loihi, MORB, and Komatiite are from Shi et al. (2022) and references therein. Data for olivine phenocrysts in Cenozoic alkaline basalts from Mongolia (Zhang et al., 2021), NE China (Chen et al., 2015a; Wang et al., 2015; Zhang and Guo, 2016; Pang et al., 2019; Liu et al., 2022), North China (Xu et al., 2012b; Liu et al., 2015b; Li et al., 2016b; Xu et al., 2017; Hong et al., 2020, 2021), and SE China (Sun et al., 2017; Zeng et al., 2017) are illustrated in Table S4.

research was then carried out to find a combination of parameters when the resultant melt composition best matched the studied basalts. The effects of a single parameter on the compositions of the resulting melts are shown in Fig. 9. After grid inspection, the best-fit combination appears to be 80% lherzolite +20% silica-deficient garnet pyroxenite in the source, a final melting depth of ~2 GPa (corresponding to a lithospheric thickness of ~66 km), ~1380 °C mantle potential temperature, and ~500 ppm source water content in the source (Fig. 10). Note that the silica-deficient pyroxenite here is KG1. In addition to KG1, the other silica-deficient pyroxenite incorporated in the software, MIX1G, has also

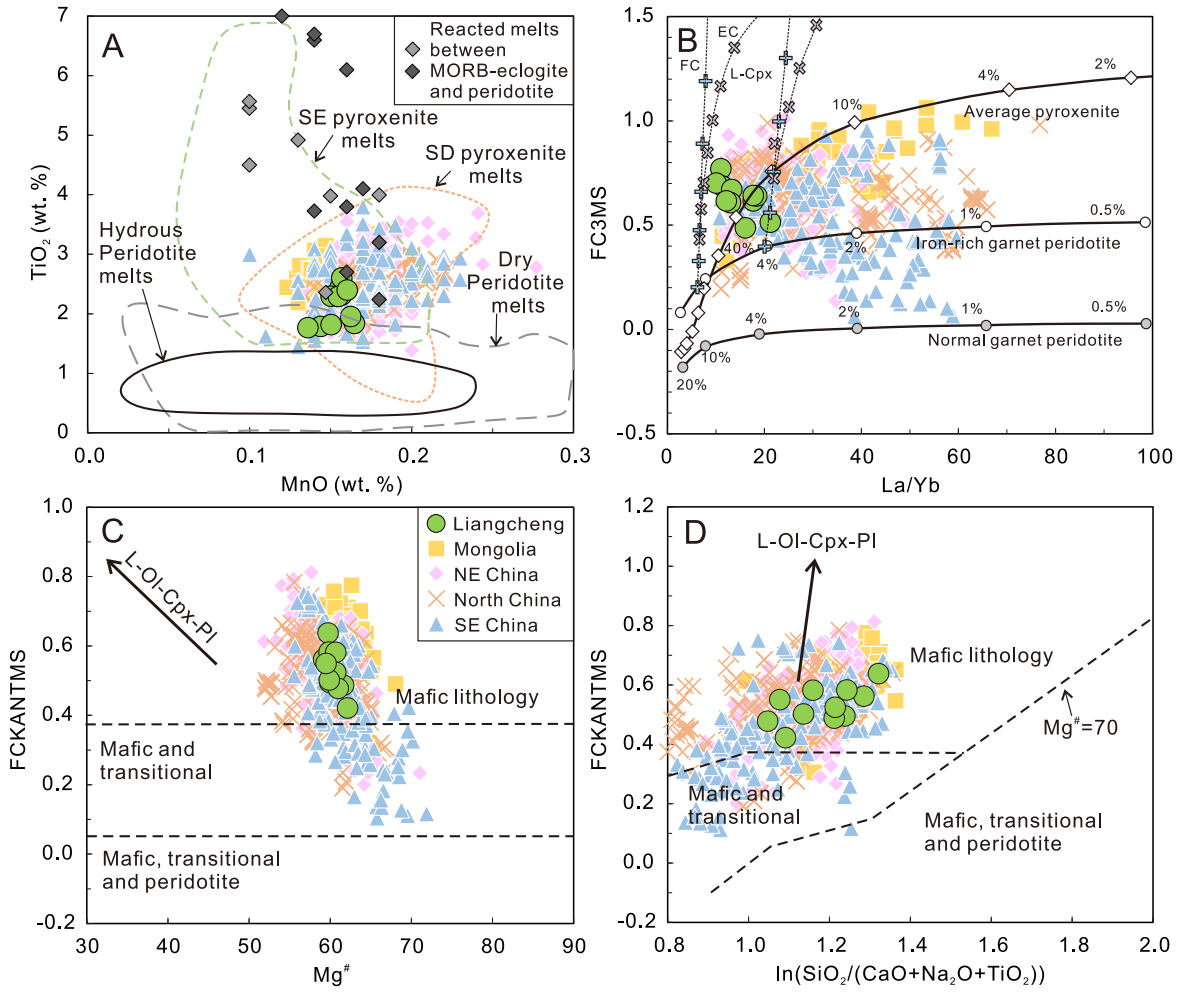

Fig. 7. (A) Whole-rock TiO_2 vs. MnO contents diagram. Sources of experimental data are identical to Liu et al. (2008a), and Ma et al. (2016). Reacted melts between MORB-eclogite and peridotite are from Mallik and Dasgupta (2012). The dark grey squares represent reacted melts obtained from the mixed runs while the light grey squares point to reacted melts acquired from the layered runs; (B) FC3MS values vs. La/Yb ratios. Variations of La/Yb ratios for experimental peridotite and pyroxenite melts are calculated through the batch melting model of Yang and Zhou (2013). The dashed lines with blue and purple cross represent Cpx fractional and equilibrium crystallization (FC and EC) by 10 wt% increments each step (Yang and zhou, 2013); FCKANTMS values vs. whole-rock Mg number ($Mg^{\#}$) (C) and ln (SiO_2/(CaO + Na_2O + TiO_2)) (D) (Yang et al., 2019). All plotted basalts have high MgO contents (≥ 8 wt%) and plot on the CO_2-free side in the CaO vs. SiO_2 diagram (Fig. S7). Data for basalts from Mongolia (Barry et al., 2003; Chuvashova et al., 2007; Savatenkov et al., 2010; Hunt et al., 2012; Yarmolyuk et al., 2015; Zhang et al., 2021), NE China (Chen et al., 2007; Chuvashova et al., 2007; Ho et al., 2008; Yan and Zhao, 2008; Zou et al., 2008; Xu et al., 2012a; Ho et al., 2013; Chen et al., 2015b; Wang et al., 2015; Yu et al., 2015; Guo et al., 2016; Zhang and Guo, 2016; Togtokh et al., 2019; He et al., 2019b; Pang et al., 2019; Lei et al., 2020), North China (Tang et al., 2006; Chen et al., 2007; Liu et al., 2008a; Chen et al., 2009b; Zhang et al., 2009; Zeng et al., 2010, 2011, 2021; Wang et al., 2011; Xu et al., 2012b, 2017; Sakuyama et al., 2013; Hong et al., 2020; Zou et al., 2022), and SE China (Zou et al., 2000; Ho et al., 2003; Zeng et al., 2013; Li et al., 2015, 2016c, 2020; Liu et al., 2016; Sun et al., 2017; Yu et al., 2019) are listed in Table S5. (For interpretation of the references to colour in this figure legend, the reader is referred to the web version of this article.)

been considered. It can be observed that the results yielded by the MIX1G model show similar variations to those of the KG1 model when changing the parameters during modeling (Fig. S8). The best-fit model acquired using MIX1G as the end member shows identical final melting pressure and water content but a higher proportion of pyroxenite in the source and lower melting temperature than the KG1 model (Fig. 10). The best-fit conditions given by the MIX1G model do not fit well with the Liangcheng basalts compared to the KG1 model, which suggests MIX1G may not be an appropriate candidate. Such a result indicates that a pyroxenite with a high proportion of relatively refractory components, like KG1, is needed in the source of Liangcheng basalts because KG1 is a mixture of peridotite and pyroxenite and contains fewer fusible components than MIX1G (Kogiso et al., 1998). The estimated melting pressure and temperature align well with those calculated by whole-rock compositions (1384 ± 17 °C and 2.2 ± 0.2 GPa) (Figs. 11, S9; Lee et al., 2009; Herzberg, 2011), and the predicted water content approximates those given by the minerals and whole-rock chemistry (550–759 ppm, see text in Supplemental Material, Figs. S10, S11, and Table S3), implying that our model is reliable. The melting temperature (~1380 °C) is significantly higher than the xenolith-based temperatures of the regional lithospheric mantle (< 1000 °C; Chen et al., 2001; Huang and Xu, 2010; Zhao et al., 2021), suggesting an asthenospheric origin. Since lithosphere may act as a passive mechanical barrier to continuous upwelling of the asthenosphere, the estimated final melting depth can be approximately treated as the melting pressure of these basalts (Niu et al., 2011). It should be noted that the melting pressure (~2 GPa, corresponding to the depth of ~66 km) is slightly lower than the regional lithospheric thickness as constrained by geophysical observations (~80 km, Chen et al., 2009a; Huang et al., 2009), which may be attributed to lithospheric thickening by asthenospheric thermal decay after basalt formation (Xu et al., 2004).

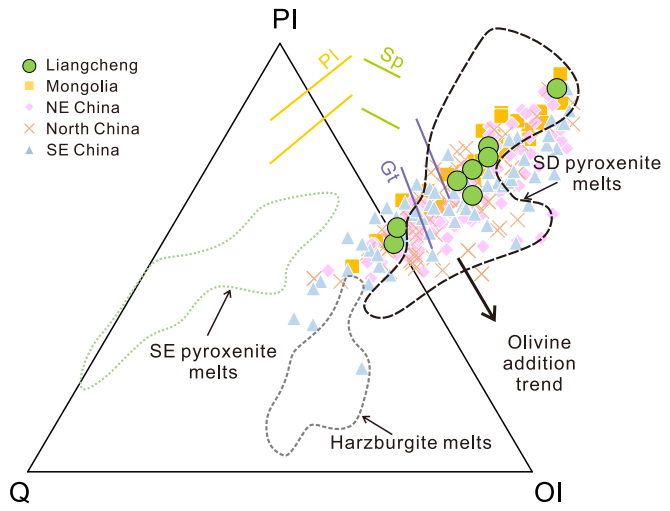

Fig. 8. Pseudoternary sub-projections for the Liangcheng basalts that only experienced olivine fractionation (Tormey et al., 1987; Grove, 1993). The predicted plagioclase (Pl), spinel (Sp), and garnet (Gt) lherzolite multiple saturation points (MSPs) as a function of increasing pressure from 1 atm to 4.0 GPa are also shown for comparison. Pl and Sp lherzolite MSPs are calculated based on the model of Till et al. (2012) and the calculation of Gt lherzolite MSPs is according to Grove et al. (2013). The pressure range for the calculation of Pl, Sp, and Gt lherzolite MSPs is 1 atm to 1.4 GPa, 1.4 to 2.4 GPa, and 2.4 to 4GPa, respectively. $Mg^{\#} = 0.73$, $NaK^{\#} = 0.283$ and 0.515, $P_2O_5 = 0.7$ wt% were used for the calculation. The three segments of each trend show compositional change of MSPs for Pl, Sp, and Gt lherzolite facies with increasing pressure. Data for experimental melts from silica-excess (SE) and silica-deficient (SD) pyroxenites as well as harzburgite are compiled in Liu et al. (2008a), and Ma et al. (2016). Data for basalts from Mongolia, NE China, North China, and NE China are shown in Table S5, and data sources are the same as those in Fig. 7.

5.4. Recycled components in the mantle source

It is widely accepted that recycled components were introduced in the mantle source of the Cenozoic basalts in Central-East Asia via subduction or delamination, and various types of recycled materials have been identified using geochemical and isotopic tools. These recycled components include continental crust, oceanic crust (both the upper and lower oceanic crust), and sediment (with or without carbonate) (Zeng et al., 2011; Xu et al., 2012a; Liu et al., 2015a, 2015b; Li et al., 2017). The Liangcheng basalts show positive Nb–Ta and negative Pb anomalies, in contrast with the continental crust (Rudnick and Gao, 2014). Instead, they are characterized by high Ce/Pb and Nb/U ratios, indicating the involvement of igneous oceanic crust. This is because subducted igneous oceanic crusts usually have high Nb/U and Ce/Pb ratios due to the preferential release of U and Pb relative to Nb and Ce during slab dehydration (Stracke et al., 2003). In addition, the absence of positive europium anomaly and positive correlation between Eu/Eu* and SiO_2 in the Liangcheng basalts suggest insignificant plagioclase accumulation in the source, thus ruling out the possibility of the involvement of lower oceanic crust (cumulate gabbro) in the source because lower oceanic crust contains abundant plagioclase and has high SiO_2 contents and relatively higher Sr, Eu concentrations than similarly incompatible elements (Xu et al., 2012a). Besides that, these basalts display enriched mantle-type OIB trace-element patterns and radiogenic Sr isotopic compositions, which may imply the incorporation of sediments into their source (Plank and Langmuir, 1998; Chauvel et al., 2008). To discriminate the types of incorporated sediments, we carried out quantitative modeling using trace elements and isotopic systematics (Fig. 12). We chose the depleted-MORB mantle (DMM), altered oceanic crust, and several kinds of sediments as endmembers; it should be noted that we did not consider carbonate-bearing sediments because carbonate plays a minor role in the source of the Liangcheng basalts as we discussed in section 5.3. The modeling results suggest that both pelagic and terrigenous sediments were involved in the mantle source of the Liangcheng basalts (Fig. 12). As a result, we conclude that recycled oceanic crust, pelagic and terrigenous sediments collectively contributed to the formation of Liangcheng basalts. These recycled enriched components melted and reacted with the ambient peridotite to form a silica-deficient pyroxenite-bearing mantle domain, which acted as a source lithology for the studied basalt.

The Central-East Asian continent has experienced multiple subduction events during the Phanerozoic (Windley et al., 2010). These subductions involve the Paleo-Tethys oceanic crust and subsequent deep subduction of the Yangtze continental crust (> 200 Ma; Wu et al., 2009), the Paleo-Asian oceanic crust (540–200 Ma; Wan et al., 2018; Jing et al., 2022), the Mongol-Okhotsk oceanic crust (> 120 Ma; Kravchinsky et al., 2002; Van der Voo et al., 2015), and the (Paleo-) Pacific oceanic crust (< 180 Ma; Ma and Xu, 2021 and references therein). Discriminating the origin of recycled components is difficult because of the cumulative effects of different tectonic events. However, we compiled olivine chemistry, whole-rock geochemical and isotopic data of Cenozoic alkaline basalts from Central-East Asia (including NE China, North China, SE China, and Mongolia; Tables S4, S5) and we found that these basalts not only have similar source lithology but also show broadly overlapping isotopic compositions (Figs. 6, 7, 8, 12), suggesting that their mantle sources may share the same origins. Consequently, we propose that subducted oceanic crusts and sediments from different subduction episodes introduced various recycled components into the asthenospheric mantle. After long periods of mantle convection and mixing, recycled components of different origins are dispersed and may serve as mantle sources for the Liangcheng basalts as well as other Cenozoic alkaline basalts in Central-East Asia. We suggest that this scenario might explain the wide similarities in the source lithology and isotopic compositions of these basalts (Figs. 6, 7, 8, 12).

5.5. Melting mechanism of the Liangcheng basalts and its implication for the generation of intraplate basaltic magmatism in Central-East Asia

Cenozoic alkaline basalts beyond the BMW have been previously interpreted as derived from localized asthenospheric upwelling due to lithospheric rifting or delamination (Barry et al., 2003; Hunt et al., 2012), large-scale convection related to mantle plume (Johnson et al., 2005), or subduction of the Pacific plate or India-Eurasia collision (Li et al., 2018; Chen and Faccenda, 2019). The Liangcheng basalts are located in the North China Craton, which experienced craton destruction during the Mesozoic (Zhu and Xu, 2019; Wu et al., 2019). Large-scale extension structures, lithospheric delamination or rifting, and associated magmatism occurred during this period (Ma and Xu, 2021), much earlier than the formation of the Cenozoic basalts. Therefore, asthenospheric upwelling triggered by lithospheric rifting or delamination is unlikely in the studied basalts. For the mantle plume hypothesis, the relatively low calculated mantle potential temperatures (<1400 °C), the absence of geophysical observations and geological and petrological evidence, such as positive thermal anomalies, progressive age migration, radiant mafic dykes, or high-$Mg^{\#}$ picrite, show no signs for the presence of a mantle plume beneath the studied area. As a consequence, the mantle plume model is not a candidate. Recently, direct mantle melting induced by subduction of the Pacific slab (Xu et al., 2018; Chen and Faccenda, 2019) or India-Eurasia collision (Li et al., 2018; Zhang et al., 2021) has been frequently suggested to explain the formation of widespread Cenozoic basalts in Central and East Asia. However, the Liangcheng area is away from the western edge of the subducted Pacific plate, as revealed by seismic images (Fig. 1B; Huang and Zhao, 2006), and can hardly be reached by mantle flow induced by the India-Eurasia collision because of the obstruction of the thick Ordos lithosphere (Yu et al., 2021). As a result, these basalts are unlikely to be directly linked to these two subduction events. Based on the above discussion, we suggest that an alternative melting mechanism is

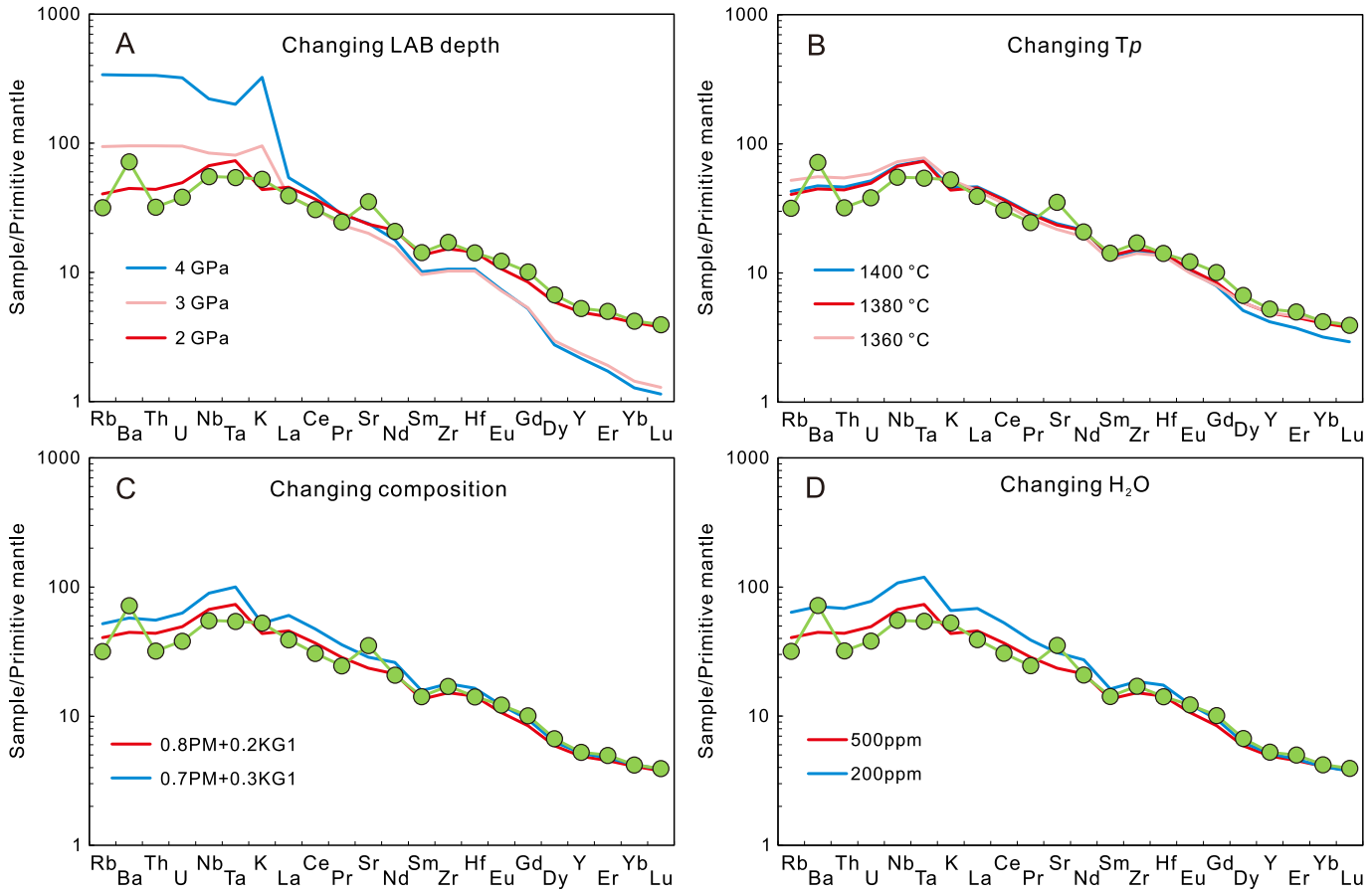

Fig. 9. Effects of mantle potential temperature, water contents, source lithologies, and final depth of melting (lithosphere-asthenosphere boundary, LAB) on the modeled melts. Also plotted is the average composition of the Liangcheng basalts (MgO ≥ 8 wt%). (A) the controlled parameters are source water content (500 ppm), source lithologies (80% PM + 20% KG1), potential temperature (1380 °C) and final melting pressure (2 GPa); (B) the controlled parameters are source water content (500 ppm), source lithologies (80% PM + 20% KG1) and final melting pressure (2 GPa); (C) the controlled parameters are source water content (500 ppm), potential temperature (1380 °C) and final melting pressure (2 GPa); (D) the controlled parameters are source lithologies (80% PM + 20% KG1), potential temperature (1380 °C) and final melting pressure (2 GPa). PM: primitive mantle (McDonough and Sun, 1995), KG1: silica-deficient pyroxenite (inserted in the REEBOX PRO program, Brown and Lesher, 2016). Abbreviations: T*p*, potential temperature; LAB, lithosphere-asthenosphere boundary. The final melting depth is controlled by the lithospheric thickness and can be approximated to the thickness of the LAB (Niu et al., 2011). (For interpretation of the references to colour in this figure legend, the reader is referred to the web version of this article.)

required to account for the generation of these basalts.

Edge-driven convection due to steps in the lithospheric structure/thickness combined with plate movement could be a feasible mechanism to explain the origin of the Liangcheng basalts. The lithosphere in the study area probably thinned before the basalt eruption based on the compositional transition from Mesozoic basalts to Cenozoic basalts (Guo et al., 2014). This inference is supported by the absence of garnet-bearing xenoliths (Zhao et al., 2021), the calculated low melting pressure of our samples and regional xenolith-bearing basalts (Xu et al.,2017), and the present lithospheric thickness determined by surface wave tomography (~80 km; Chen et al., 2009a; Huang et al., 2009). In addition, S-receiver function images have revealed that the lithospheric thickness of the western NCC is characterized by significant lateral variations, which is 200 km in the Ordos block and sharply thinned to 80 km in the Yinchuan-Hetao and Shaanxi-Shanxi rift areas over a lateral distance of <200–400 km (Chen et al., 2009a). Such abrupt and significant changes in lithospheric thickness, combined with the disturbance from deep subduction of the Pacific plate, would efficiently cause edge-driven convection of the asthenosphere beneath the NCC, especially if the viscosity of the asthenospheric mantle was lowered by melts and volatiles released from the Pacific plate, as has been suggested by a recent numerical modeling study (Sun and Liu, 2023). Since the Liangcheng area locates in the joint of the Yinchuan-Hetao and Shaanxi-Shanxi rift system with a thin lithosphere and is adjacent to the Ordos block, it is, therefore, in a propitious tectonic situation to trigger edge-driven convection. In this case, decompression melting of the asthenospheric mantle would occur when mantle convection drives fusible mantle domains from areas with relatively thick lithosphere to those that have thin ones.

The Liangcheng basalts share many similarities with many other Cenozoic alkaline basalts in Central-East Asia, especially those with high MgO (≥ 8 wt%) and plotted on the CO_2-free side in the CaO vs. SiO_2 diagrams (Fig. S7). These similarities include: 1) the geological distribution patterns in which these basalts are preferentially developed along deep major faults or weak zones between stable blocks (Fig. 1A); 2) they all have silica-deficient pyroxenite in the source (Figs. 6, 7, 8); 3) they yield low melting pressure (Fig. 11, <3 GPa); 4) similar recycled components such as oceanic crust and sediment (both pelagic and terrigenous) existed in their mantle source (Fig. 12). Although some basalts with extreme geochemical signatures (nephelinites and potassic/ultrapotassic basalts) may have distinct origins (mantle transition zone, Sakuyama et al., 2013; Wang et al., 2017; Xu et al., 2020; Zeng et al., 2021), most of the alkaline basalts in Central-East Asia generally have overlapping geochemical features and similar source components and melting conditions (Figs. 6, 7, 11, 12). These characteristics are difficult to reconcile with those of previous models, including mantle plumes,

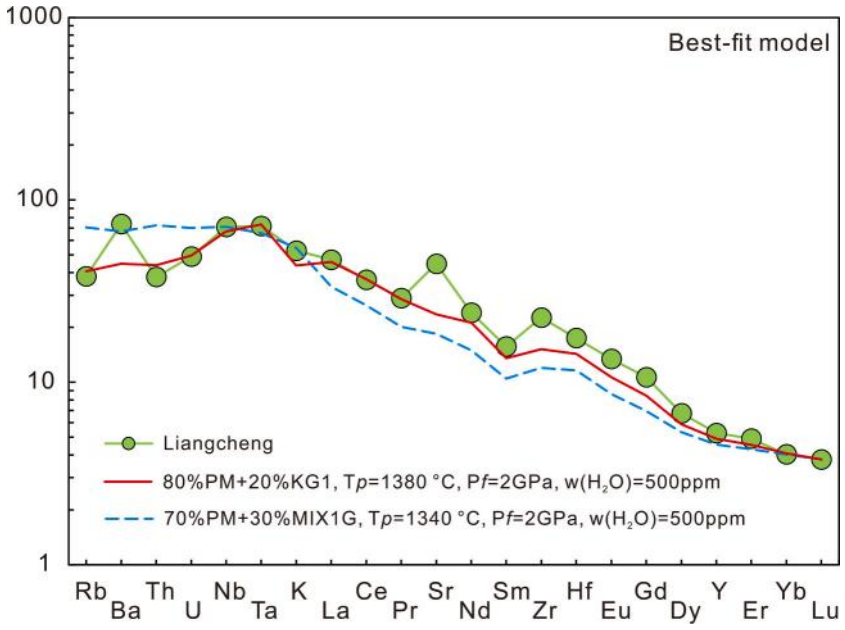

Fig. 10. Modeled melt compositions that best fit the averaged Liangcheng basalts (MgO ≥ 8 wt%) (Brown and Lesher, 2016). KG1 and MIX1G represent the end-member of silica-deficient pyroxenite and PM represents the primitive mantle. (For interpretation of the references to colour in this figure legend, the reader is referred to the web version of this article.)

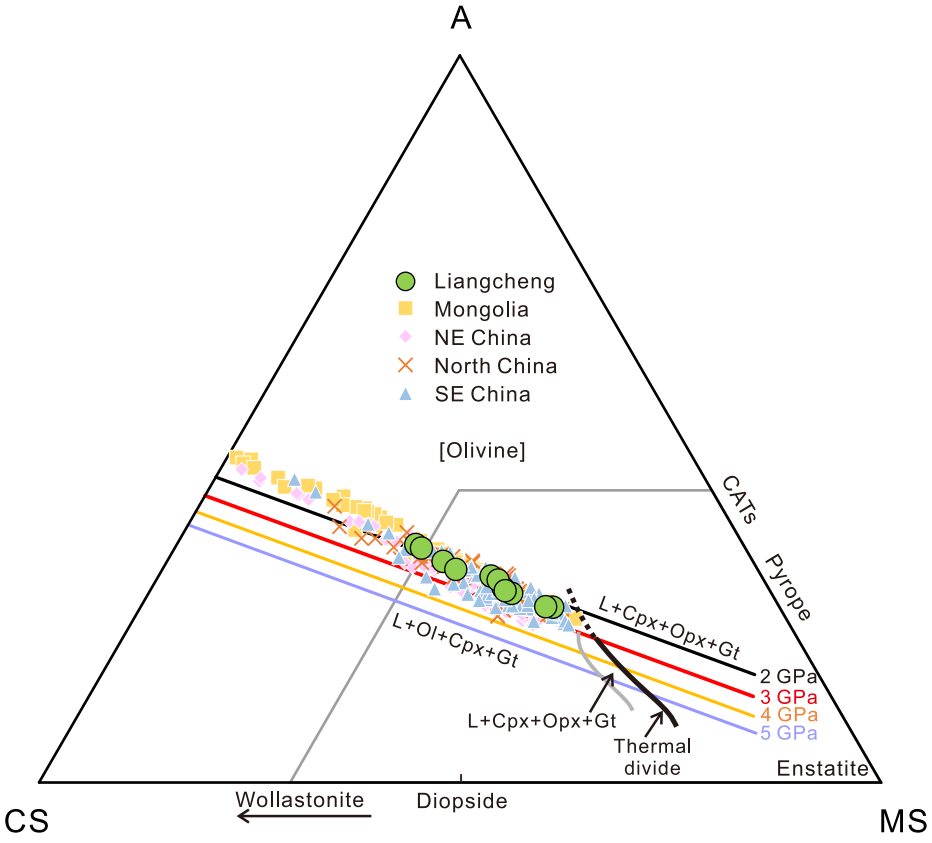

Fig. 11. A mole% pseudo ternary projection from or toward olivine into the CS-MS-A plane (Herzberg, 2011). The projection code follows O'Hara (1968), and the calculation method of cotectics is from Herzberg (2011). Abbreviations: L-liquid, Ol-olivine, Q-quartz, Cpx-clinopyroxene, Opx-orthopyroxene, Gt-garnet. All plotted basalts have high MgO contents (≥ 8 wt%) and plot on the CO_2-free side in the CaO vs. SiO_2 diagram (Fig. S7). Data for basalts from Mongolia, NE China, North China, and NE China are shown in Table S5, and data sources are identical to those in Fig. 7.

lithospheric rifting or delamination, or plate subduction. Instead, these similarities are likely the result of decompression melting of small-scale mantle convection due to regional lithospheric thickness variations. This proposal is consistent with recent studies suggesting that small-scale mantle convection driven by regional lithospheric thickness variations may have occurred beneath SE and NE China (Xu et al., 2022; Zhou et al., 2023). Similar small-scale convection has also been detected in the Baikal rift zone of Central Asia by geophysical observations and proposed to account for the intraplate magmatism in regions with thin lithosphere and sharp thickness variations, such as Southeast Australia, North America, and West Africa (Missenard and Cadoux, 2012; Davies and Rawlinson, 2014; Ballmer et al., 2015). Based on the above

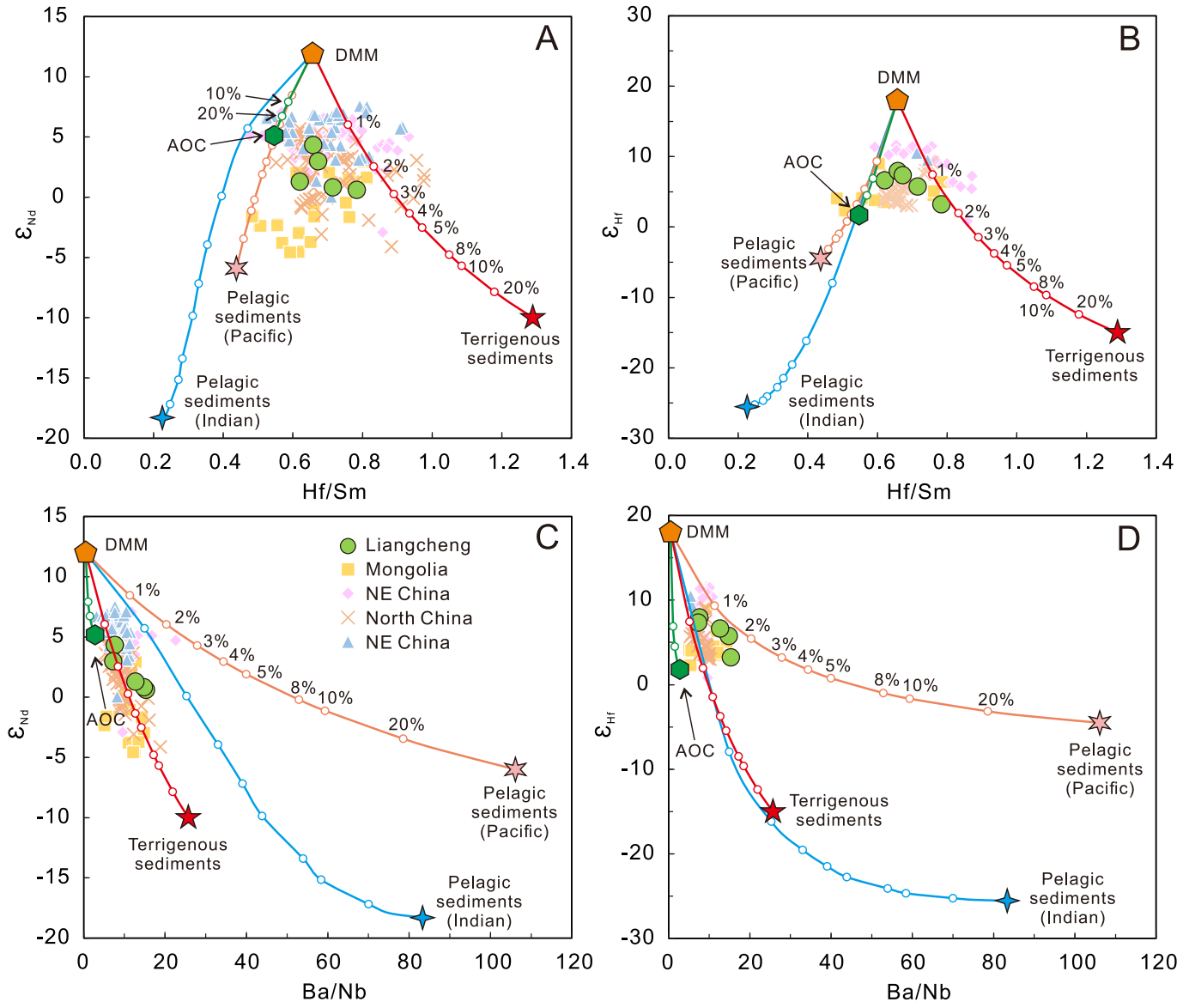

Fig. 12. (A) ε_{Nd} vs. Hf/Sm, (B) ε_{Hf} vs. Hf/Sm, (C) ε_{Nd} vs. Ba/Nb, (D) ε_{Hf} vs. Ba/Nb diagrams for the Liangcheng basalts. DMM is from Workman and Hart (2005); Altered oceanic crust (AOC) is from Rehka and Hofmann (1997) and Guo et al. (2009); Pelagic sediments from the western Pacific and Indian Ocean are according to Cousens et al. (1994) and Rehka and Hofmann (1997), respectively. Terrigenous sediment is from Wedepohl (1995) and Chauvel et al. (2014). Data for Cenozoic alkaline basalts from Mongolia, NE China, North China, and NE China are listed in Table S5, and data sources are the same as those in Fig. 7.

considerations, we suggest that edge-driven convection may be ubiquitous beneath Central-East Asia and probably plays an important role in the formation of pervasive Cenozoic small-volume alkaline basalts.

6. Conclusions

We conducted comprehensive geochemical studies and thermodynamic modeling of the Liangcheng basalts to explore the source characteristics and melting mechanisms of continental intraplate alkaline basalts beyond the Big Mantle Wedge. These basalts have a silica-deficient pyroxenite-bearing mantle source (20% silica-deficient pyroxenite +80% peridotite) with melting pressures and temperatures of ~2GPa and 1380 °C, respectively. Considering the relatively low melting pressure, regional lithospheric thickness variations, and tectonic history, we propose that edge-driven convection could be a likely mechanism for the studied basalts. Similar source characteristics, melting conditions, and geological distribution patterns between the Liangcheng basalt and many other regional Cenozoic alkaline basalts, combined with similar lithospheric thickness variations observed beneath these basalts, suggest that edge-driven convection may be ubiquitous beneath Central-East Asia and that such a melting mechanism could serve as a major driving force for widespread continental intraplate basaltic magmatism.

Declaration of Competing Interest

The authors declare that they have no known competing financial interests or personal relationships that could have appeared to influence the work reported in this paper.

Data availability

Data will be made available on request.

Acknowledgment

We are grateful to the journal science editor Dr. Sonja Aulbach and two anonymous reviewers for their critical and constructive comments, which substantially improved an earlier version of this manuscript. We also thank Xiao Ma and Wen-Mei Liu for their assistance during the whole-rock major elements analysis and Dr. Jiang-Gu Lu for her kind instruction during the EPMA experiment. This study was financially supported by the National Key Technologies R&D Program (2019YFA0708603 and 2016YFC0600403), and the National Natural Science Foundation of China (NSFC) (41973033 and 41673034).

Appendix A. Supplementary data

Supplementary data to this article can be found online at https://doi.org/10.1016/j.chemgeo.2023.121537.

References

Baker, J., Peate, D., Waight, T., Meyzen, C., 2004. Pb isotopic analysis of standards and samples using a ^{207}Pb-^{204}Pb double spike and thallium to correct for mass bias with a double-focusing MC-ICP-MS. Chem. Geol. 211 (3–4), 275–303. https://doi.org/10.1016/j.chemgeo.2004.06.030.

Ballmer, M.D., Conrad, C.P., Smith, E.I., Harmon, N., 2013. Non-hotspot volcano chains produced by migration of shear-driven upwelling toward the East Pacific Rise. Geology 41 (4), 479–482. https://doi.org/10.1130/G33804.1.

Ballmer, M.D., Conrad, C.P., Smith, E.I., Johnsen, R., 2015. Intraplate volcanism at the edges of the Colorado Plateau sustained by a combination of triggered edge-driven convection and shear-driven upwelling. Geochem. Geophys. Geosyst. 16, 366–379. https://doi.org/10.1002/2014GC005641.

Barry, T.L., Saunders, A.D., Kempton, P.D., Windley, B.F., Pringle, M.S., Dorjnamjaa, D., Saandar, S., 2003. Petrogenesis of Cenozoic basalts from Mongolia: evidence for the role of asthenospheric versus metasomatized lithospheric mantle sources. J. Petrol. 44 (1), 55–91. https://doi.org/10.1093/petrology/44.1.55.

Bédard, J.H., 2006. A catalytic delamination-driven model for coupled genesis of Archean crust and subcontinental lithospheric mantle. Geochim. Cosmochim. Acta 70 (5), 1188–1214. https://doi.org/10.1016/j.gca.2005.11.008.

Brown, E.L., Lesher, C.E., 2016. REEBOX PRO: a forward model simulating melting of thermally and lithologically variable upwelling mantle. Geochem. Geophys. Geosyst. 17, 3929–3968. https://doi.org/10.1002/2016GC006579.

Brown, E.L., Petersen, K.D., Lesher, C.E., 2020. Markov chain Monte Carlo inversion of mantle temperature and source composition, with application to Reykjanes Peninsula, Iceland. Earth Planet. Sci. Lett. 532, 116007 https://doi.org/10.1016/j.epsl.2019.116007.

Bryan, S.E., Ernst, R.E., 2008. Revised definition of large igneous provinces (LIPs). Earth Sci. Rev. 86, 175–202. https://doi.org/10.1016/j.earscirev.2007.08.008.

Cai, R.H., Xu, S., Ionov, D.A., Huang, J., Liu, S.A., Li, S.G., Liu, J.G., 2022. Carbonated big Mantle Wedge Extending to the NE Edge of the Stagnant Pacific Slab: Constraints from late Mesozoic-Cenozoic Basalts from Far Eastern Russia. J. Earth Sci. 33 (1), 121–132. https://doi.org/10.1007/s12583-021-1516-x.

Chauvel, C., Lewin, E., Carpentier, M., Arndt, N.T., Marini, J.C., 2008. Role of recycled oceanic basalt and sediment in generating the Hf-Nd mantle array. Nat. Geosci. 1, 64–67. https://doi.org/10.1038/ngeo.2007.51.

Chauvel, C., Garçon, M., Bureau, S., Besnault, A., Jahn, B.M., Ding, Z.L., 2014. Constraints from loess on the Hf-Nd isotopic composition of the upper continental crust. Earth Planet. Sci. Lett. 388, 48–58. https://doi.org/10.1016/j.epsl.2013.11.045.

Chen, L., Faccenda, M., 2019. Subduction-induced upwelling of a hydrous transition zone: Implications for the Cenozoic magmatism in Northeast China. Journal of Geophysical Research: Solid Earth 124, 11489–11504. https://doi.org/10.1029/2019JB018133.

Chen, S.H., O'Reilly, S.Y., Zhou, X.H., Griffin, W.L., Zhang, G.H., Sun, M., Feng, J.L., Zhang, M., 2001. Thermal and petrological structure of the lithosphere beneath Hannuoba, Sino-Korean Craton, China: evidence from xenoliths. Lithos 56 (4), 267–301. https://doi.org/10.1016/S0024-4937(00)00065-7.

Chen, Y., Zhang, Y.X., Graham, D., Su, S.G., Deng, J.F., 2007. Geochemistry of Cenozoic basalts and mantle xenoliths in Northeast China. Lithos 96 (1–2), 108–126. https://doi.org/10.1016/j.lithos.2006.09.015.

Chen, L., Cheng, C., Wei, Z., 2009a. Seismic evidence for significant lateral variations in lithospheric thickness beneath the central and western North China Craton. Earth Planet. Sci. Lett. 286 (1), 171–183. https://doi.org/10.1016/j.epsl.2009.06.022.

Chen, L.H., Zeng, G., Jiang, S.Y., Hofmann, A.W., Xu, X.S., 2009b. Sources of Anfengshan basalts: subducted lower crust in the Sulu UHP belt, China. Earth Planet. Sci. Lett. 286, 426–435. https://doi.org/10.1016/j.epsl.2009.07.006.

Chen, J.Y., Yang, J.H., Zhang, J.H., Sun, J.F., Wilde, S.A., 2013. Petrogenesis of the Cretaceous Zhangzhou batholith in southeastern China: Zircon U–Pb age and Sr–Nd–Hf–O isotopic evidence. Lithos 162–163, 140–156. https://doi.org/10.1016/j.lithos.2013.01.003.

Chen, H., Xia, Q.K., Ingrin, J., Jia, Z.B., Feng, M., 2015a. Changing recycled oceanic components in the mantle source of the Shuangliao Cenozoic basalts, NE China: new constraints from water content. Tectonophysics 650, 113–123. https://doi.org/10.1016/j.tecto.2014.07.022.

Chen, S.S., Fan, Q.C., Zou, H.B., Zhao, Y.W., Shi, R.D., 2015b. Geochemical and Sr–Nd isotopic constraints on the petrogenesis of late Cenozoic basalts from the Abaga area, Inner Mongolia, eastern China. J. Volcanol. Geotherm. Res. 305, 30–44. https://doi.org/10.1016/j.jvolgeores.2015.09.018.

Chen, H., Xia, Q.K., Ingrin, J., Deloule, E., Bi, Y., 2017. Heterogeneous source components of intraplate basalts from NE China induced by the ongoing Pacific slab subduction. Earth Planet. Sci. Lett. 459, 208–220. https://doi.org/10.1016/j.epsl.2016.11.030.

Chuvashova, I.S., Rasskazov, S.V., Ysnygina, T.A., Saranina, E.V., Fefelov, N.N., 2007. Holocene volcanism in Central Mongolia and Northeast China: Asynchronous decompressional and fluid melting of the mantle. J. Volcanol. Seismol. 1 (6), 372–396. https://doi.org/10.1134/S0742046307060024.

Connolly, J.A.D., 1990. Multivariable phase Diagrams: An algrorithm based on generalized thermodynamics. Am. J. Sci. 290, 666–718. https://doi.org/10.2475/ajs.290.6.666.

Connolly, J.A.D., 2005. Computation of phase equilibria by linear programming: a tool for geodynamic modeling and its application to subduction zone decarbonation. Earth Planet. Sci. Lett. 236, 524–541. https://doi.org/10.1016/j.epsl.2005.04.033.

Conrad, C., Bianco, T.A., Smith, E.I., Wessel, P., 2011. Patterns of intraplate volcanism controlled by asthenospheric shear. Nat. Geosci. 4, 317–321. https://doi.org/10.1038/ngeo1111.

Cousens, B.L., Allan, J.F., Gorton, M.P., 1994. Subduction-modified pelagic sediments as the enriched component in back-arc basalts from the Japan Sea: Ocean Drilling Program sites 797 and 794. Contrib. Mineral. Petrol. 117, 421–434. https://doi.org/10.1007/BF00307275.

Dai, H.K., Zheng, J.P., Griffin, W.L., O'Reilly, S.Y., Xiong, Q., Ping, X.Q., Chen, F.K., Lu, J.G., 2020. Pyroxenite xenoliths record complex melt impregnation in the deep lithosphere of the northwestern North China Craton. J. Petrol. 62 (2), 1–32. https://doi.org/10.1093/petrology/egaa079.

Davies, J.H., Bunge, H., 2006. Are splash plumes the origin of minor hotspots? Geology 34, 349–352. https://doi.org/10.1130/G22193.1.

Davies, D.R., Rawlinson, N.P., 2014. On the origin of recent intraplate volcanism in Australia. Geology 42, 1031–1034. https://doi.org/10.1130/G36093.1.

Foley, S.F., Prelevic, D., Rehfeldt, T., Jacob, D.E., 2013. Minor and trace elements in olivines as probes into early igneous and mantle melting processes. Earth Planet. Sci. Lett. 363, 181–191. https://doi.org/10.1016/j.epsl.2012.11.025.

Gale, A., Dalton, C.A., Langmuir, C.H., Su, Y., Schilling, J.G., 2013. The mean composition of ocean ridge basalts. Geochem. Geophys. Geosyst. 14, 489–518. https://doi.org/10.1029/2012GC004334.

Grove, T.L., 1993. Corrections to expressions for calculating mineral components in"Origin of calc-alkaline series lavas at Medicine Lake Volcano by fractionation, assimilation and mixing" and "Experimental petrology of normal MORB near the Kane Fracture Zone: 22o-25oN, mid-Atlantic ridge". Contrib. Mineral. Petrol. 114, 422–424. https://doi.org/10.1007/BF01046543.

Grove, T.L., Holbig, E.S., Barr, J.A., Till, C.B., Krawczynski, M.J., 2013. Melts of garnet lherzolite: experiments, models, and comparison to melts of pyroxenite and carbonated lherzolite. Contrib. Mineral. Petrol. 166 (3), 887–910. https://doi.org/10.1007/s00410-013-0899-9.

Guo, F., Fan, W.M., Li, C.W., Miao, L.C., Zhao, L., 2009. Early Paleozoic subduction of the Paleo-Asian Ocean: geochronological and geochemical evidence from the Dashizhai basalts, Inner Mongolia. Chin. Sci. Bull. 39, 940–951. https://doi.org/10.1007/s11430-009-0083-2 (In Chinese with English abstract).

Guo, P.Y., Niu, Y.L., Ye, L., Liu, J.J., Sun, P., Cui, H.X., Zhang, Y., Gao, J., Su, L., Zhao, J.X., Feng, Y.X., 2014. Lithosphere thinning beneath west North China Craton: evidence from geochemical and Sr–Nd–Hf isotope compositions of Jining basalts. Lithos 202–203, 37–54. https://doi.org/10.1016/j.lithos.2014.04.024.

Guo, P.Y., Niu, Y.L., Sun, P., Ye, L., Liu, J.J., Zhang, Y., Fang, Y.X., Zhao, J.X., 2016. The origin of Cenozoic basalts from Central Inner Mongolia, East China: the consequence of recent mantle metasomatism genetically associated with seismically observed paleo-Pacific slab in the mantle transition zone. Lithos 240, 104–118. https://doi.org/10.1016/j.lithos.2015.11.010.

Guo, P.Y., Niu, Y.L., Sun, P., Gong, H.M., Wang, X.H., 2020. Lithosphere thickness controls continental basalt compositions: An illustration using Cenozoic basalts from eastern China. Geology 48, 128–133. https://doi.org/10.1130/G46710.1.

He, Y.S., Meng, X.N., Ke, S., Wu, H.J., Zhu, C.W., Teng, F.Z., Hoefs, J., Huang, J., Yang, W., Xu, L.J., Hou, Z.H., Ren, Z.Y., Li, S.G., 2019a. A nephelinitic component with unusual $\delta^{56}Fe$ in Cenozoic basalts from eastern China and its implications for deep oxygen in Cenozoic basalts from eastern China and its implications for deep oxygen cycle. Earth Planet. Sci. Lett. 512, 175–183. https://doi.org/10.1016/j.epsl.2019.02.009.

He, Y., Chen, L.H., Shi, J.H., Zeng, G., Wang, X.J., Xue, X.Q., Zhong, Y., Erdmann, S., Xie, L.W., 2019b. Light Mg isotopic composition in the mantle beyond the big Mantle Wedge beneath eastern Asia. Journal of Geophysical Research: Solid Earth 124. https://doi.org/10.1029/2018JB016857.

Herzberg, C.T., 2011. Identification of source lithology in the Hawaiian and Canary Islands: implication for origins. J. Petrol. 52 (1), 113–146. https://doi.org/10.1093/petrology/egq075.

Herzberg, C., Asimow, P.D., 2008. Petrology of some oceanic island basalts: PRIMELT2.XLS software for primary magma calculation. Geochem. Geophys. Geosyst. 9, 09001. https://doi.org/10.1029/2008GC002057.

Ho, K.S., Chen, J.C., Lo, C.H., Zhao, H.L., 2003. ^{40}Ar–^{39}Ar dating and geochemical characteristics of late Cenozoic basaltic rocks from the Zhejiang–Fujian region, SE China: eruption ages, magma evolution and petrogenesis. Chem. Geol. 197, 287–318. https://doi.org/10.1016/S0009-2541(02)00399-6.

Ho, K.S., Liu, Y., Chen, J.C., Yang, H.J., 2008. Elemental and Sr-Nd-Pb isotopic compositions of late Cenozoic Abaga basalts, Inner Mongolia: Implications for petrogenesis and mantle process. Geochem. J. 42 (4), 339–357. https://doi.org/10.2343/geochemj.42.339.

Ho, K.S., Ge, W.C., Chen, J.C., You, C.F., Yang, H.J., Zhang, Y.L., 2013. Late Cenozoic magmatic transitions in the central Great Xing'an Range, Northeast China: geochemical and isotopic constraints on petrogenesis. Chem. Geol. 352, 1–18. https://doi.org/10.1016/j.chemgeo.2013.05.040.

Hoernle, K., White, J.D.L., Bogaard, P.V.D., Hauff, F., Coombs, D.S., Werner, R., Timm, C., Garbe-Schönberg, D., Reay, A., Cooper, A.F., 2006. Cenozoic intraplate volcanism on New Zealand: Upwelling induced by lithospheric removal. Earth Planet. Sci. Lett. 248, 350–367. https://doi.org/10.1016/j.epsl.2006.06.001.

Hong, L.B., Xu, Y.G., Zhang, L., Wang, Y., Ma, L., 2020. Recycled carbonate-induced oxidization of the convective mantle beneath Jiaodong, Eastern China. Lithos 366–367, 105544. https://doi.org/10.1016/j.lithos.2020.105544.

Hong, L.B., Zhang, Y.H., Zhang, L., Xu, Y.G., Liu, Z., He, P.L., 2021. Olivine chemistry of the Quaternary Datong basalts of the Trans-North China Orogen: insights into mantle source lithology and redox–hydration state. Geol. Soc. Lond., Spec. Publ. 510, 115–131. https://doi.org/10.1144/SP510-2020-142.

Howarth, G.H., Harris, C., 2017. Discriminating between pyroxenite and peridotite sources for continental flood basalts (CFB) in southern Africa using olivine chemistry. Earth Planet. Sci. Lett. 475, 143–151. https://doi.org/10.1016/j.epsl.2017.07.043.

Huang, X.L., Xu, Y.G., 2010. Thermal state and structure of the lithosphere beneath Eastern China: a synthesis on basalt-borne xenoliths. J. Earth Sci. 21 (5), 711–730. https://doi.org/10.1007/s12583-010-0111-3.

Huang, J.L., Zhao, D.P., 2006. High-resolution mantle topography of China and surrounding regions. J. Geophys. Res. Solid Earth 111, B09305. https://doi.org/10.1029/2005JB004066.

Huang, Z.X., Li, H.Y., Zheng, Y.J., Peng, Y.J., 2009. The lithosphere of North China Craton from surface wave tomography. Earth Planet. Sci. Lett. 288, 164–173. https://doi.org/10.1016/j.epsl.2009.09.019.

Huang, J., Li, S.G., Xiao, Y., Ke, S., Li, W.Y., Tian, Y., 2015. Origin of low δ^{26}Mg Cenozoic basalts from South China Block and their geodynamic implications. Geochim. Cosmochim. Acta 164, 298–317. https://doi.org/10.1016/j.gca.2015.04.054.

Hunt, A.C., Parkinson, I.J., Harris, N.B.W., Barry, T.L., Rogers, N.W., Yondon, M., 2012. Cenozoic volcanism on the Hangai dome, Central Mongolia: Geochemical evidence for changing melt sources and implications for mechanisms of melting. J. Petrol. 53, 1913–1942. https://doi.org/10.1093/petrology/egs038.

Ionov, D., 2002. Mantle structure and rifting processes in the Baikal-Mongolia region: geophysical data and evidence from xenoliths in volcanic rocks. Tectonophysics 351, 41–60. https://doi.org/10.1016/s0040-1951(02)00124-5.

Jing, Y., Yang, H., Ge, W.C., Dong, Y., Ji, Z., Bi, J.H., Zhou, H.Y., Xing, D.H., 2022. When did the final closure occur of the eastern Paleo-Asian Ocean: Constraints from the latest Early–Middle Triassic adakitic granites in the southeastern Central Asian Orogenic Belt. Gondwana Res. 103, 146–171. https://doi.org/10.1016/j.gr.2021.08.001.

Johnson, J.S., Gibson, S.A., Thompson, R.N., Nowell, G.M., 2005. Volcanism in the Vitim Volcanic Field, Siberia: Geochemical evidence for a mantle plume beneath the Baikal Rift Zone. J. Petrol. 46, 1309–1344. https://doi.org/10.1093/petrology/egi016.

Kawabata, H., Hanyu, T., Chang, Q., Kimura, J.I., Nichols, A.R.L., Tatsumi, Y., 2011. The petrology and geochemistry of St. Helena Alkali Basalts: evaluation of the oceanic crust-recycling model for HIMU OIB. J. Petrol. 52, 791–838. https://doi.org/10.1093/petrology/egr003.

King, S.D., Ritsema, J., 2000. African hot spot volcanism: small-scale convection in the upper mantle beneath cratons. Science 290, 1137–1140. https://doi.org/10.1126/science.290.5494.1137.

Kogiso, T., Hirose, K., Takahahshi, E., 1998. Melting experiments on homogeneous mixtures of peridotite and basalt: application to the genesis of ocean island basalts. Earth Planet. Sci. Lett. 162, 45–61. https://doi.org/10.1016/S0012-821X(98)00156-3.

Kravchinsky, V.A., Cogné, J.P., Harbert, W.P., Kuzmin, M.I., 2002. Evolution of the Mongol–Okhotsk Ocean as constrained by new palaeomagnetic data from the Mongol–Okhotsk suture zone, Siberia. Geophys. J. Int. 148, 34–57. https://doi.org/10.1046/j.1365-246x.2002.01557.x.

Kuritani, T., Ohtani, E., Kimura, J.I., 2011. Intensive hydration of the mantle transition zone beneath China caused by slab stagnation. Nat. Geosci. 4, 713–716. https://doi.org/10.1038/NGEO1250.

Lambart, S., Laporte, D., Schiano, P., 2013. Markers of the pyroxenite contribution in the major-element compositions of oceanic basalts: Review of the experimental constraints. Lithos 160–161, 14–36. https://doi.org/10.1016/j.lithos.2012.11.018.

Lambart, S., Baker, M.B., Stolper, E.M., 2016. The role of pyroxenite in basalt genesis: Melt-PX, a melting parameterization for mantle pyroxenites between 0.9 and 5 GPa. J. Geophys. Res. Solid Earth 121, 5708–5735. https://doi.org/10.1002/2015JB012762.

Lambart, S., Hamilton, S., Lang, O.I., 2022. Compositional variability of San Carlos olivine. Chem. Geol. 605, 120968 https://doi.org/10.1016/j.chemgeo.2022.120968.

Le Bas, M.J., Le Maitre, R.W., Streckeisen, A., Zanettin, B., 1986. A chemical classification of volcanic rocks based on the total alkali-silica diagram. J. Petrol. 27, 745–750. https://doi.org/10.1093/petrology/27.3.745.

Le Roux, V., Lee, C.T.A., Turner, S.J., 2010. Zn/Fe systematics in mafic and ultramafic systems: Implications for detecting major element heterogeneities in the Earth's mantle. Geochim. Cosmochim. Acta 74, 2779–2796. https://doi.org/10.1016/j.gca.2010.02.004.

Lee, C.T., Luffi, P., Plank, T., Dalton, H., Leeman, W., 2009. Constraints on the depths and temperatures of basaltic magma generation on Earth and other terrestrial planets using new thermobarometers for mafic magmas. Earth Planet. Sci. Lett. 279 (1–2), 20–33. https://doi.org/10.1016/j.epsl.2008.12.020.

Lei, M., Guo, Z.F., Zhao, W.B., Zhang, M.L., Ma, L., 2020. Coexisting late Cenozoic Potassic and Sodic Basalts in NE China: Role of Recycled Oceanic Components in Intraplate Magmatism and Mantle Heterogeneity. Lithosphere 1, 8875012. https://doi.org/10.2113/2020/8875012.

Li, D.M., Li, Q., 2003. Serial K-Ar Dating along the Volcanic Section in Zuoyun, Shanxi Province. Acta Geosci. Sin. 24 (6), 559–562 (In Chinese with English abstract).

Li, C.F., Li, X.H., Li, Q.L., Guo, J.H., Yang, Y.H., 2012. Rapid and precise determination of Sr and Nd isotopic ratios in geological samples from the same filament loading by thermal ionization mass spectrometry employing a single-step separation scheme. Anal. Chim. Acta 727, 54–60. https://doi.org/10.1016/j.aca.2012.03.040.

Li, Y.Q., Ma, C.Q., Robinson, P.T., Zhou, Q., Liu, M.L., 2015. Recycling of oceanic crust from a stagnant slab in the mantle transition zone: evidence from Cenozoic continental basalts in Zhejiang Province, SE China. Lithos 230, 146–165. https://doi.org/10.1016/j.lithos.2015.05.021.

Li, J., Tang, S.H., Zhu, X.K., Pan, C.X., 2016a. Production and Certification of the Reference Material GSB 04-3258-2015 as a ^{143}Nd/^{144}Nd Isotope Ratio Reference. Geostand. Geoanal. Res. 41, 255–262. https://doi.org/10.1111/ggr.12151.

Li, H.Y., Xu, Y.G., Ryan, J.G., Huang, X.L., Ren, Z.Y., Guo, H., Ning, Z.G., 2016b. Olivine and melt inclusion chemical constraints on the source of intracontinental basalts from the eastern North China Craton: discrimination of contributions from the subducted Pacific slab. Geochim. Cosmochim. Acta 178, 1–19. https://doi.org/10.1016/j.gca.2015.12.032.

Li, Y.Q., Ma, C.Q., Robinson, P.T., 2016c. Petrology and geochemistry of Cenozoic intraplate basalts in east–Central China: Constraints on recycling of an oceanic slab in the source region. Lithos 262, 27–43. https://doi.org/10.1016/j.lithos.2016.06.012.

Li, S.G., Yang, W., Ke, S., Meng, X., Tian, H., Xu, L., He, Y., Huang, J., Wang, X.C., Xia, Q., Sun, W., Yang, X., Ren, Z.Y., Wei, H., Liu, Y., Meng, F., Yan, J., 2017. Deep carbon cycles constrained by a large-scale mantle Mg isotope anomaly in eastern China. Natl. Sci. Rev. 4, 111–120. https://doi.org/10.1093/nsr/nww070.

Li, S.L., Guo, Z., Chen, Y.S.J., Yang, Y.J., Huang, Q.H., 2018. Lithospheric structure of the Northern Ordos from Ambient noise and teleseismic surface wave tomography. J. Geophys. Res. Solid Earth 123, 6940–6957. https://doi.org/10.1029/2017JB015256.

Li, Y.Q., Kitagawa, H., Nakamura, E., Ma, C.Q., Hu, X.Y., Kobayashi, K., Sakaguchi, C., 2020. Various ages of recycled material in the source of Cenozoic basalts in SE China: Implications for the role of the Hainan plume. J. Petrol. 61 (6), egaa060 https://doi.org/10.1093/petrology/egaa060.

Liu, Y.S., Gao, S., Yuan, H.L., Zhou, L., Liu, X.M., Wang, X.C., Hu, Z.C., Wang, L.S., 2004. U-Pb zircon ages and Nd, Sr, and Pb isotopes of lower crustal xenoliths from North China Craton: insight on evolution of lower continental crust. Chem. Geol. 211, 87–109. https://doi.org/10.1016/j.chemgeo.2004.06.023.

Liu, Y.S., Gao, S., Kelemen, P.B., Xu, W.L., 2008a. Recycled crust controls contrasting source compositions of Mesozoic and Cenozoic basalts in the North China Craton. Geochim. Cosmochim. Acta 72 (9), 2349–2376. https://doi.org/10.1016/j.gca.2008.02.018.

Liu, Y.S., Zong, K.Q., Kelemen, P.B., Gao, S., 2008b. Geochemistry and magmatic history of eclogites and ultramafic rocks from the Chinese continental scientific drill hole: subduction and ultrahigh-pressure metamorphism of lower crustal cumulates. Chem. Geol. 247 (1), 133–153. https://doi.org/10.1016/j.chemgeo.2007.10.016.

Liu, Y.S., Gao, S., Hu, Z.C., Gao, C.G., Zong, K.Q., Wang, D.B., 2010. Continental and oceanic crust recycling-induced melt-peridotite interactions in the Trans-North China Orogen: U-Pb dating, Hf isotopes and trace elements in zircons of mantle xenoliths. J. Petrol. 51 (1–2), 537–571. https://doi.org/10.1093/petrology/egp082.

Liu, J., Xia, Q.K., Deloule, E., Chen, H., Feng, M., 2015a. Recycled oceanic crust and marine sediment in the source of alkali basalts in Shandong, eastern China: evidence from magma water content and oxygen isotopes. J. Geophys. Res. Solid Earth 120, 8281–8303. https://doi.org/10.1002/2015JB012476.

Liu, J., Xia, Q.K., Deloule, E., Ingrin, J., Chen, H., Feng, M., 2015b. Water content and oxygen isotopic composition of alkali basalts from the Taihang Mountains, China: Recycled oceanic components in the mantle source. J. Petrol. 56, 681–702. https://doi.org/10.1093/petrology/egv013.

Liu, X.J., Xu, J.F., Xiao, W.J., Castillo, P.R., Shi, Y., Wang, S.Q., Huo, Q.Y., Feng, Z.H., 2015c. The boundary between the Central Asian Orogenic belt and Tethyan tectonic domain deduced from Pb isotopic data. J. Asian Earth Sci. 113 (1), 7–15. https://doi.org/10.1016/j.jseaes.2015.04.039.

Liu, S.C., Xia, Q.K., Choi, S.H., Deloule, E., Li, P., Liu, J., 2016. Continuous supply of recycled Pacific oceanic materials in the source of Cenozoic basalts in SE China: the Zhejiang case. Contrib. Mineral. Petrol. 171, 100. https://doi.org/10.1007/s00410-016-1310-4.

Liu, J.Q., Chen, L.H., Wang, X.J., Zhang, H.L., Zeng, G., Erdmann, S., Zhang, L., Ren, Z.Y., 2022. Olivine and melt inclusion chemical constraints on the nature and origin of the common mantle component beneath eastern Asia. Contrib. Mineral. Petrol. 177, 116. https://doi.org/10.1007/s00410-022-01981-y.

Ma, Q., Xu, Y.G., 2021. Magmatic perspective on subduction of Paleo-Pacific plate and initiation of big mantle wedge in East Asia. Earth Sci. Rev. 213, 103473 https://doi.org/10.1016/j.earscire2020.103473.

Ma, Q., Zheng, J.P., Griffin, W.L., Zhang, M., Tang, H.Y., Su, Y.P., Ping, X.Q., 2012. Triassic "adakitic" rocks in an extensional setting (North China): melts from the cratonic lower crust. Lithos 149, 159–173. https://doi.org/10.1016/j.lithos.2012.04.017.

Ma, Q., Xu, Y.G., Zheng, J.P., Griffin, W.L., Hong, L.B., Ma, L., 2016. Coexisting early cretaceous high-Mg andesites and adakitic rocks in the North China Craton: the role

of water in intraplate magmatism and cratonic destruction. J. Petrol. 57 (7), 1279–1308. https://doi.org/10.1093/petrology/egw040.
Mallik, A., Dasgupta, R., 2012. Reaction between MORB-eclogite derived melts and fertile peridotite and generation of ocean island basalts. Earth Planet. Sci. Lett. 329–330, 97–108. https://doi.org/10.1016/j.epsl.2012.02.007.
Matzen, A.K., Wood, B.J., Baker, M.B., Stolper, E.M., 2017. The roles of pyroxenite and peridotite in the mantle sources of oceanic basalts. Nat. Geosci. 10, 530–535. https://doi.org/10.1038/NGEO2968.
McDonough, W.F., Sun, S.S., 1995. The composition of the Earth. Chem. Geol. 120 (3–4), 223–253. https://doi.org/10.1016/0009-2541(94)00140-4.
McGee, L.E., Smith, I.E.M., 2016. Interpreting chemical compositions of small-scale basaltic systems: a review. J. Volcanol. Geotherm. Res. 325, 45–60. https://doi.org/10.1016/j.jvolgeores.2016.06.007.
Missenard, Y., Cadoux, A., 2012. Can Moroccan Atlas lithospheric thinning and volcanism be induced by edge-driven convection? Terra Nova 24, 27–33. https://doi.org/10.1111/j.1365-3121.2011.01033.x.
Niu, Y.L., Wilson, M., Humphreys, E.R., O'Hara, M.J., 2011. The origin of intra-plate ocean island basalts (OIB): the lid effect and its geodynamic implications. J. Petrol. 52, 1443–1468. https://doi.org/10.1093/petrology/egr030.
O'Hara, M.J., 1968. The bearing of phase equilibria studies in synthetic and natural systems on the origin and evolution of basic and ultrabasic rocks. Earth Sci. Rev. 4, 69–133. https://doi.org/10.1016/0012-8252(68)90147-5.
Oliveira, B., Afonso, J.C., Klöcking, M., 2021. Melting conditions and mantle source composition from probabilistic joint inversion of major and rare earth element concentrations. Geochim. Cosmochim. Acta 315, 251–275. https://doi.org/10.1016/j.gca.2021.09.008.
Pang, C.J., Wang, X.C., Li, C.F., Wilde, S.A., Tian, L., 2019. Pyroxenite-derived Cenozoic basaltic magmatism in Central Inner Mongolia, eastern China: potential contributions from the subduction of the Paleo-Pacific and Paleo-Asian oceanic slabs in the Mantle transition Zone. Lithos 332, 39–54. https://doi.org/10.1016/j.lithos.2019.02.012.
Plank, T., Langmuir, C.H., 1998. The chemical composition of subducting sediment and its consequences for the crust and mantle. Chem. Geol. 145, 325–394. https://doi.org/10.1016/S0009-2541(97)00150-2.
Polat, A., Hofmann, A.W., Rosing, M.T., 2002. Boninite-like volcanic rocks in the 3.7–3.8 Ga Isua greenstone belt, West Greenland: geochemical evidence for intra-oceanic subduction zone processes in the early Earth. Chem. Geol. 184, 231–254. https://doi.org/10.1016/S0009-2541(01)00363-1.
Rehka, M., Hofmann, A.W., 1997. Recycled Ocean crust and sediment in Indian Ocean MORB. Earth Planet. Sci. Lett. 147 (1), 93–106. https://doi.org/10.1016/S0012-821X(97)00009-5.
Roeder, P.L., Emslie, R.F., 1970. Olivine–liquid equilibrium. Contrib. Mineral. Petrol. 29, 275–289. https://doi.org/10.1007/BF00371276.
Rudnick, R.L., Gao, S., 2014. Composition of the continental crust. In: Holland, H.D., Turekian, K.K. (Eds.), Treatise on Geochemistry, , Second Editionvol. 3, pp. 1–64. https://doi.org/10.1016/B978-0-08-095975-7.00301-6.
Sakuyama, T., Tian, W., Kimura, J.I., Fukao, Y., Hirahara, Y., Takahashi, T., Senda, R., Chang, Q., Miyazaki, T., Obayashi, M., Kawabata, H., Tatsumi, Y., 2013. Melting of dehydrated oceanic crust from the stagnant slab and of the hydrated mantle transition zone: Constraints from Cenozoic alkaline basalts in eastern China. Chem. Geol. 359, 32–48. https://doi.org/10.1016/j.chemgeo.2013.09.012.
Savatenkov, V.M., Yarmolyuk, V.V., Kudryashova, E.A., Kozlovskii, A.M., 2010. Sources and Geodynamics of the late Cenozoic Volcanism of Central Mongolia: evidence from Isotope-Geochemical Studies. Petrology 18 (3), 297–327. https://doi.org/10.1134/S0869591110030057.
Sheldrick, T.C., Hahn, G., Ducea, M.N., Stoica, A.M., Constenius, K., Heizler, M., 2020a. Peridotite versus pyroxenite input in Mongolian Mesozoic-Cenozoic lavas, and dykes. Lithos 376–377, 105747. https://doi.org/10.1016/j.lithos.2020.105747.
Sheldrick, T.C., Barry, T.L., Dash, B., Gan, C., Millar, I.L., Barfod, D.N., Halton, A.M., 2020b. Simultaneous and extensive removal of the East Asian lithospheric root. Sci. Rep. 10 (1), 1–6. https://doi.org/10.1038/s41598-020-60925-3.
Shi, J.H., Zeng, G., Chen, L.H., Hanyu, T., Wang, X.J., Zhong, Y., Xie, L.W., Xie, W.L., 2022. An eclogitic component in the Pitcairn mantle plume: evidence from olivine compositions and Fe isotopes of basalts. Geochim. Cosmochim. Acta 318, 415–427. https://doi.org/10.1016/j.gca.2021.12.017.
Sobolev, A.V., Hofmann, A.W., Sobolev, S.V., Nikogosian, I.K., 2005. An olivine-free mantle source of Hawaiian shield basalts. Nature 434, 590–597. https://doi.org/10.1038/nature03411.
Stracke, A., Bizimis, M., Salters, V.J.M., 2003. Recycling oceanic crust: Quantitative constraints. Geochem. Geophys. Geosyst. 4, 3. https://doi.org/10.1029/2001GC000223.
Sun, Y.J., Liu, M., 2023. Edge-driven asthenospheric convection beneath the North China Craton: a numerical study. Tectonophysics 849, 229726. https://doi.org/10.1016/j.tecto.2023.229726.
Sun, S.S., McDonough, W.F., 1989. Chemical and isotopic systematics of oceanic basalts: implications for mantle composition and processes. Geol. Soc. Lond. Spec. Publ. 42, 313–345. https://doi.org/10.1144/GSL.SP.1989.042.01.19.
Sun, P., Niu, Y.L., Guo, P.Y., Duan, M., Wang, X.H., Gong, H.M., Xiao, Y.Y., 2020. The lithospheric thickness control on the compositional variation of continental intraplate basalts: a demonstration using the Cenozoic basalts and Clinopyroxene Megacrysts from Eastern China. J. Geophys. Res. Solid Earth 125, e2019JB019315. https://doi.org/10.1029/2019JB019315.
Sun, P., Niu, Y.L., Guo, P.Y., Ye, L., Liu, J.J., Feng, Y.X., 2017. Elemental and Sr– Nd–Pb isotope geochemistry of the Cenozoic basalts in Southeast China: insights into their mantle sources and melting processes. Lithos 272–273, 16–30. https://doi.org/10.1016/j.lithos.2016.12.005.
Tang, Y.J., Zhang, H.F., Ying, J.F., 2006. Asthenosphere–lithospheric mantle interaction in an extensional regime: implication from the geochemistry of Cenozoic basalts from Taihang Mountains, North China Craton. Chem. Geol. 233, 309–327. https://doi.org/10.1016/j.chemgeo.2006.03.013.
Thirlwall, M.F., 1991. Long-term reproducibility of multicollector Sr and Nd isotope ratio analysis. Chem. Geol. 94, 85–104. https://doi.org/10.1016/S0009-2541(10)80021-X.
Till, C.B., Grove, T.L., Krawczynski, M.J., 2012. A melting model for variably depleted and enriched lherzolite in the plagioclase and spinel stability. J. Geophys. Res. Solid Earth 117, B06206. https://doi.org/10.1029/2011JB009044.
Togtokh, K., Miao, L.C., Zhang, F.C., Baatar, M., Anaad, C., Bars, A., 2019. Major, trace element, and Sr-Nd isotopic geochemistry of Cenozoic basalts in Central-North and East Mongolia: Petrogenesis and tectonic implication. Geochem. J. 54, 3660–3680. https://doi.org/10.1002/gj.3331.
Tormey, D.R., Grove, T.L., Bryan, W.B., 1987. Experimental petrology of normal MORB near the Kane Fracture Zone: 22°–25°N, mid-Atlantic ridge. Contrib. Mineral. Petrol. 96, 121–139. https://doi.org/10.1007/BF00375227.
Van der Voo, R., van Hinsbergen, D.J., Domeier, M., Spakman, W., Torsvik, T.H., 2015. Latest Jurassic-earliest cretaceous closure of the Mongol-Okhotsk Ocean: a palaeomagnetic and seismological-tomographic analysis. Geol. Soc. Am. Spec. Pap. 513, 589–606. https://doi.org/10.1130/2015.2513(19).
Wan, B., Li, S.H., Xiao, W.J., Windley, B.F., 2018. Where and when did the Paleo-Asian ocean form? Precambrian Res. 317, 241–252. https://doi.org/10.1016/j.precamres.2018.09.003.
Wang, Y., Zhao, Z.F., Zheng, Y.F., Zhang, J.J., 2011. Geochemical constraints on the nature of mantle source for Cenozoic continental basalts in east-Central China. Lithos 125, 940–955. https://doi.org/10.1016/j.lithos.2011.05.007.
Wang, X.C., Wilde, S.A., Li, Q.L., Yang, Y.N., 2015. Continental flood basalts derived from the hydrous mantle transition zone. Nat. Commun. 6, 7700. https://doi.org/10.1038/ncomms8700.
Wang, X.J., Chen, L.H., Hofmann, A.W., Mao, F.G., Liu, J.Q., Zhong, Y., 2017. Mantle transition zone-derived EM1 component beneath NE China: Geochemical evidence from Cenozoic potassic basalts. Earth Planet. Sci. Lett. 465, 16–28. https://doi.org/10.1016/j.epsl.2017.02.028.
Zhao, X.M., Wang, H., Li, Z.H., Evans, N.J., Ying, J.F., Yang, Y.H., Zhang, H.F., 2021. Nature and evolution of lithospheric mantle beneath the western North China Craton: constraints from peridotite and pyroxenite xenoliths in the Sanyitang basalts. Lithos 384–385, 105987. https://doi.org/10.1016/j.lithos.2021.105987.
Wedepohl, K.H., 1995. The composition of the continental crust. Geochim. Cosmochim. Acta 59, 1217–1232. https://doi.org/10.1016/0016-7037(95)00038-2.
Weis, D., Kieffer, B., Maerschalk, C., Barling, J., Jong, J.D., Williams, G.A., Hanano, D., Pretorius, W., Mattielli, N., Scoates, J.S., Goolaerts, A., Friedman, R.M., Mahoney, J.B., 2006. High-precision isotopic characterization of USGS reference materials by TIMS and MC-ICP-MS. Geochem. Geophys. Geosyst. 7 (8), 139–149. https://doi.org/10.1029/2006GC001283.
Weis, D., Kieffer, B., Hanano, D., Nobre Silva, I., Barling, J., Pretorius, W., Maerschalk, C., Mattielli, N., 2007. Hf isotope compositions of U.S. Geological Survey reference materials. Geochem. Geophys. Geosyst. 8 (6), 1–15. https://doi.org/10.1029/2006GC001473.
Willbold, M., Stracke, A., 2006. Trace element composition of mantle end-members: implications for recycling of oceanic and upper and lower continental crust. Geochem. Geophys. Geosyst. 7, Q4004. https://doi.org/10.1029/2005GC001005.
Windley, B.F., Maruyama, S., Xiao, W.J., 2010. Delamination/thinning of sub-continental lithospheric mantle under eastern China: the role water and multiple subduction. Am. J. Sci. 310, 1250–1293. https://doi.org/10.2475/10.2010.03.
Workman, R.K., Hart, S.R., 2005. Major and trace element composition of the depleted MORB mantle (DMM). Earth Planet. Sci. Lett. 231 (1–2), 53–72. https://doi.org/10.1016/j.epsl.2004.12.005.
Workman, R.K., Hart, S.R., Jackson, M., Regelous, M., Farley, K.A., Blusztajn, J., Kurz, M., Staudigel, H., 2004. Recycled metasomatized lithosphere as the origin of the Enriched Mantle II (EM2) end-member: evidence from the Samoan Volcanic Chain. Geochem. Geophys. Geosyst. 5, 1–44. https://doi.org/10.1029/2003GC000623.
Wu, Y.B., Hanchar, J.M., Gao, S., Sylvester, P.J., Tubrett, M., Qiu, H.N., Wijbrans, J.R., Brouwer, F.M., Yang, S.H., Yang, Q.J., Liu, Y.S., Yuan, H.L., 2009. Age and nature of eclogites in the Huwan shear zone, and the multi-stage evolution of the Qinling-Dabie-Sulu Orogen, Central China. Earth Planet. Sci. Lett. 277 (3–4), 345–354. https://doi.org/10.1016/j.epsl.2008.10.031.
Wu, F.Y., Yang, J.H., Xu, Y.G., Wilde, S.A., Walker, R.J., 2019. Destruction of the North China craton in the Mesozoic. Annu. Rev. Earth Planet. Sci. 47, 173–195. https://doi.org/10.1146/annurev-earth-053018-060342.
Xiao, W.J., Windley, B.F., Sun, S., Li, J.L., Huang, B.C., Han, C.M., Yuan, C., Sun, M., Chen, H.L., 2015. A tale of amalgamation of three Permo-Triassic college systems in Central Asia: Oroclines, sutures, and terminal accretion. Annu. Rev. Earth Planet. Sci. 43, 477–507. https://doi.org/10.1146/annurev-earth-060614-105254.
Xu, Z., Zheng, Y.F., 2019. Crust-Mantle Interaction in the Paleo-Pacific Subduction Zone: Geochemical evidence from Cenozoic Continental Basalts in Eastern China. Earth Sci. 44 (12), 4135–4143 (In Chinese with English abstract). https://doi.org/10.3799/dqkx.2019.273 (In Chinese with English abstract).
Xu, Y.G., Chung, S.L., Ma, J., Shi, L., 2004. Contrasting Cenozoic lithospheric evolution and architecture in western and eastern Sino–Korean Craton: constraints from geochemistry of basalts and mantle xenoliths. J. Geol. 112, 593–605. https://doi.org/10.1086/422668.
Xu, Y.G., Zhang, H.H., Qiu, H.N., Ge, W.C., Wu, F.Y., 2012a. Oceanic crust components in continental basalts from Shuangliao, Northeast China: derived from the mantle

transition zone? Chem. Geol. 328, 168–184. https://doi.org/10.1016/j.chemgeo.2012.01.027.
Xu, Z., Zhao, Z.F., Zheng, Y.F., 2012b. Slab-mantle interaction for thinning of cratonic lithospheric mantle in North China: geochemical evidence from Cenozoic continental basalts in Central Shandong. Lithos 146, 202–217. https://doi.org/10.1016/j.lithos.2012.05.019.
Xu, R., Liu, Y.S., Wang, X.H., Zong, K.Q., Hu, Z.C., Chen, H.H., Zhou, L., 2017. Crust recycling induced compositional-temporal-spatial variations of Cenozoic basalts in the Trans-North China Orogen. Lithos 274–275, 383–396. https://doi.org/10.1016/j.lithos.2016.12.024.
Xu, Y.G., Li, H.Y., Hong, L.B., Ma, L., Ma, Q., Sun, M.D., 2018. Generation of Cenozoic intraplate basalts in the big mantle wedge under eastern Asia. Sci. China Earth Sci. 61 (7), 869–886. https://doi.org/10.1007/s11430-017-9192-y.
Xu, R., Liu, Y.S., Wang, X.C., Foley, S.F., Zhang, Y.F., Yuan, H.Y., 2020. Generation of continental intraplate alkali basalts and implications for deep carbon cycle. Earth Sci. Rev. 201, 103073 https://doi.org/10.1016/j.earscire2019.103073.
Xu, R., Liu, Y.S., Lambart, S., Hoernle, K., Zhu, Y.T., Zou, Z.Q., Zhang, J.B., Wang, Z.C., Li, M., Moynier, F., Zong, K.Q., Chen, H.H., Hu, Z.C., 2022. Decoupled Zn-Sr-Nd isotopic composition of continental intraplate basalts caused by two-stage melting process. Geochim. Cosmochim. Acta 326, 234–252. https://doi.org/10.1016/j.gca.2022.03.014.
Yan, J., Zhao, J.X., 2008. Cenozoic alkali basalts from Jingpohu, NE China: the role of lithosphere-asthenosphere interaction. J. Asian Earth Sci. 33, 106–121. https://doi.org/10.1016/j.jseaes.2007.11.001.
Yang, Z.F., Zhou, J.H., 2013. Can we identify source lithology of basalt? Sci. Rep. 3 (1856), 1–15. https://doi.org/10.1038/srep01856.
Yang, W., Teng, F.Z., Zhang, H.F., Li, S.G., 2012. Magnesium isotopic systematics of continental basalts from the North China craton: Implications for tracing subducted carbonate in the mantle. Chem. Geol. 328, 185–194. https://doi.org/10.1016/j.chemgeo.2012.05.018.
Yang, Z.F., Li, J., Jiang, Q.B., Xu, F., Guo, S.Y., Li, Y., Zhang, J., 2019. Using major element logratios to recognize compositional patterns of basalt: Implications for source lithological and compositional heterogeneities. J. Geophys. Res. Solid Earth 124 (4), 3458–3490. https://doi.org/10.1029/2018JB016145.
Yarmolyuk, V.V., Kudryashova, E.A., Kozlovsky, A.M., Lebedev, V.A., Savatenkov, V.M., 2015. Late Mesozoic–Cenozoic intraplate magmatism in Central Asia and its relation with mantle diapirism: evidence from the South Khangai volcanic region, Mongolia. J. Asian Earth Sci. 111, 604–623. https://doi.org/10.1016/j.jseaes.2015.05.008.
Yu, X., Lee, C.T.A., Chen, L.H., Zeng, G., 2015. Magmatic recharge in continental flood basalts: Insights from the Chifeng igneous province in Inner Mongolia. Geochem. Geophys. Geosyst. 16, 2082–2096. https://doi.org/10.1002/2015GC005805.
Yu, X., Zeng, G., Chen, L.H., Wang, X.J., Liu, J.Q., Xie, L.W., Yang, T., 2019. Evidence for rutile-bearing eclogite in the mantle sources of the Cenozoic Zhejiang basalts, eastern China. Lithos 324–325, 152–164. https://doi.org/10.1016/j.lithos.2018.11.003.
Yu, Y., Chen, Y.S.J., Feng, Y.G., An, M.J., Liang, X.F., Guo, Z., Qu, W.L., Li, S.L., Dong, S.W., 2021. Asthenospheric flow channel from northeastern Tibet imaged by seismic tomography between Ordos block and Yangtze craton. Geophys. Res. Lett. 48, e2021GL093561 https://doi.org/10.1029/2021GL093561.
Zeng, G., Chen, L.H., Xu, X.S., Jiang, S.Y., Hofmann, A.W., 2010. Carbonated mantle sources for Cenozoic intra-plate alkaline basalts in Shandong, North China. Chem. Geol. 273, 35–45. https://doi.org/10.1016/j.chemgeo.2010.02.009.
Zeng, G., Chen, L.H., Hofmann, A.W., Jiang, S.Y., Xu, X.S., 2011. Crust recycling in the sources of two parallel volcanic chains in Shandong, North China. Earth Planet. Sci. Lett. 302, 359–368. https://doi.org/10.1016/j.epsl.2010.12.026.
Zeng, G., Chen, L.H., Hu, S.L., Xu, X.S., Yang, L.F., 2013. Genesis of Cenozoic low-ca alkaline basalts in the Nanjing basaltic field, eastern China: the case for mantle xenolith-magma interaction. Geochem. Geophys. Geosyst. 14, 1660–1677. https://doi.org/10.1002/ggge.20127.
Zeng, G., Chen, L.H., Yu, X., Liu, J.Q., Xu, X.S., Erdmann, S., 2017. Magma-magma interaction in the mantle beneath eastern China. Journal of Geophysical Research: Solid Earth 122, 2763–2769. https://doi.org/10.1002/2017JB014023.
Zeng, G., Chen, L.H., Hofmann, A.W., Wang, X.J., Liu, J.Q., Yu, X., Xie, L.W., 2021. Nephelinites in eastern China originating from the mantle transition zone. Chem. Geol. 576, 120276 https://doi.org/10.1016/j.chemgeo.2021.120276.
Zhang, M.L., Guo, Z.F., 2016. Origin of late Cenozoic Abaga-Dalinuoer basalts, eastern China: Implications for a mixed pyroxenite-peridotite source related with deep subduction of the Pacific slab. Gondwana Res. 37, 130–151. https://doi.org/10.1016/j.gr.2016.05.014.
Zhang, J.J., Zheng, Y.F., Zhao, Z.F., 2009. Geochemical evidence for interaction between oceanic crust and lithospheric mantle in the origin of Cenozoic continental basalts in east-Central China. Lithos 110, 305–326. https://doi.org/10.1016/j.lithos.2009.01.006.
Zhang, H.F., Sun, Y.L., Tang, Y.J., Xiao, Y., Zhang, W.H., Zhao, X.M., Menzies, M.A., 2012. Melt-peridotite interaction in the Pre-Cambrian mantle beneath the western North China Craton: petrology, geochemistry and Sr, Nd and Re isotopes. Lithos 149, 100–114. https://doi.org/10.1016/j.lithos.2012.01.027.
Zhang, Y.Y., Yuan, C., Huang, Z.Y., Narantsetseg, T., Ren, Z.Y., Li, P.F., Zhang, Q.L., 2021. Contrasting compositions between phenocrystic and xenocrystic olivines in the Cenozoic basalts from Central Mongolia: Constraints on source lithology and regional uplift. Am. Mineral. 106, 251–264. https://doi.org/10.2138/am-2020-7431.
Zhao, D.P., Lei, J.S., Tang, R.Y., 2004. Origin of the Changbai intraplate volcanism in Northeast China: evidence from seismic tomography. Chin. Sci. Bull. 49, 1401–1408. https://doi.org/10.1360/04wd0125.
Zhou, Z.K., Wang, D.L., Wang, T.Q., Weng, A.H., Li, Y.B., Guo, J.H., Wang, X.Q., 2023. Undulating electrical lithosphere–asthenosphere boundary beneath Northeast China; as revealed by long–period magnetotelluric data. Tectonophysics 851, 229770. https://doi.org/10.1016/j.tecto.2023.229770.
Zhu, R.X., Xu, Y.G., 2019. The subduction of the West Pacific plate and the destruction of the North China Craton. Sci. China Earth Sci. 62, 1340–1350. https://doi.org/10.1007/s11430-018-9356-y.
Zou, H.B., Zindler, A., Xu, X.S., Qi, Q., 2000. Major, trace element, and Nd, Sr and Pb isotope studies of Cenozoic basalts in SE China: mantle sources, regional variations, and tectonic significance. Chem. Geol. 171 (1–2), 33–47. https://doi.org/10.1016/S0009-2541(00)00243-6.
Zou, H.B., Fan, Q.C., Yao, Y.P., 2008. U–Th systematics of dispersed young volcanoes in NE China: Asthenosphere upwelling caused by piling up and upward thickening of stagnant Pacific slab. Chem. Geol. 255, 134–142. https://doi.org/10.1016/j.chemgeo.2008.06.022.
Zou, Z.Q., Wang, Z.C., Foley, S., Xu, R., Geng, X.L., Liu, Y.N., Liu, Y.S., Hu, Z.C., 2022. Origin of low-MgO primitive intraplate alkaline basalts from partial melting of carbonate-bearing eclogite sources. Geochim. Cosmochim. Acta 324, 240–261. https://doi.org/10.1016/j.gca.2022.02.022.